SSRG International Journal of Civil Engineering
ISSN: 2348-8352/ https://doi.org/10.14445/23488352/IJCE-V13I11P102

Volume 13 Issue 11, 16-43, November 2026
© 2026 Seventh Sense Research Group®

Original Article

Deep Learning-based Spatial Analysis of THM-Informed Degradation in Unstabilized Rammed Earth Walls

Chaymae Salhi[1], Mouna El Mkhalet[2], Nouzha Lamdouar[3]

[1,2,3]*Civil Engineering and Construction Structure GCC laboratory, Mohammadia School of Engineers EMI, Mohammed V University, Rabat, Morocco.*

[1]*Corresponding Author: chaymae.salhi@research.emi.ac.ma*

Received: 29 June 2026 Revised: 04 October 2026 Accepted: 20 October 2026 Published: 27 November 2026

Abstract *- Performance assessment of Unstabilized Rammed Earth (URE) has long relied on costly numerical simulations or destructive testing. To address this challenge, this study proposes a Deep Learning (DL) surrogate framework for predicting Thermo-Hydro-Mechanical (THM) degradation in URE walls. A synthetic dataset of 2,000 URE samples was generated using a 5-channel input tensor composed of the normalized temperature field, relative humidity field, structural texture, initial elastic modulus, and applied strain. The corresponding stress responses were computed using a two-dimensional plane-stress finite-element stage, allowing equilibrium-consistent global and spatial stress targets to be obtained. Two DL architectures were evaluated: a Convolutional Neural Network (CNN) for global scalar prediction and a U-Net for spatial damage and stress-field prediction. The CNN achieved high accuracy for global damage prediction, with an overall R^2 of 0.995, MAE of 0.011, and RMSE of 0.013. For global FEA stress prediction, the CNN achieved a moderate overall R^2 of 0.324 and RMSE of 0.305 MPa, indicating that scalar stress prediction is more challenging than damage estimation. The U-Net achieved good spatial agreement for both damage and FEA-derived stress maps, with overall SSIM values of 0.855 and 0.860, respectively. These results show that the CNN accurately reproduces the prescribed strain-defined global damage target, while spatial U-Net mapping can reproduce the heterogeneous distribution of FEA-derived stress fields. The proposed framework provides a computational proof of concept for THM-informed assessment of URE degradation and demonstrates the potential of DL surrogates to approximate FEA-derived mechanical responses after training.*

Keywords *- Unstabilized Rammed Earth, Convolutional Neural Network, U-Net architecture, Thermo-Hydro-Mechanical (THM) coupling, Structural defect segmentation.*

1. Introduction

Earthen construction has regained significant attention as a sustainable alternative to conventional high-carbon building materials, particularly in the context of circular construction, low embodied energy, and reduced dependence on cementitious binders [1-3]. Among earthen techniques, Rammed Earth (RE) is especially attractive because it can use locally available soils and provide favorable thermal inertia and hygrothermal buffering capacity [4]. URE is of particular interest because it preserves the ecological advantages of RE by avoiding cement stabilization, which can substantially increase embodied energy and carbon emissions [2, 3, 5]. However, the absence of stabilizers also increases the sensitivity of URE to soil composition, particle-size distribution, moisture state, compaction conditions, density, fabric, and specimen geometry [2, 5, 6]. As a result, URE is generally treated as a heterogeneous compacted geomaterial whose mechanical response may exhibit quasi-brittle behavior, anisotropy, and significant variability in compressive, tensile, and shear properties [2, 5, 6]. These characteristics make reliable mechanical characterization essential for the safe use of URE in modern structural applications [5, 6].

The mechanical behavior of RE has therefore been widely investigated through experimental and numerical approaches, with particular attention to compressive strength, elastic modulus, shear resistance, failure mechanisms, density effects, and the influence of manufacturing parameters [2, 5, 6]. For instance, Ávila et al. [5] combined laboratory experiments and finite element simulations to evaluate the compressive and shear properties of URE, and proposed that experimental characterization and numerical prediction tools must be integrated. In 2026, the authors further found that the mechanical response of URE is affected by multiscale factors related to soil characteristics, fabric, and

This is an open access article under the CC BY-NC-ND license (http://creativecommons.org/licenses/by-nc-nd/4.0/)

specimen configuration, and that single-parameter characterization has clear limitations [6]. Taken together, these findings support the core consensus that URE cannot be assessed solely by its global compressive strength, as its macroscopic performance arises from the interactions of local compaction, texture, suction, stiffness, and progressive damage mechanisms.

The flaws of existing traditional characterization methods have been confirmed by multiple studies: the outcomes of Ávila et al. [5, 6] and Waibel et al. [7], a study that proposes a hybrid CNN-LSTM DL model to predict the dynamic hygrothermal properties of RE from short-term data, all point out that traditional methods are time-consuming, highly material-specific, and difficult to popularize across variable soil environments.

Studies conducted across different years have also continuously demonstrated the influence of environmental factors: in 2009, Jaquin et al. [8] identified suction as a major factor affecting URE strength; in 2012, Beckett and Augarde [9] confirmed that temperature and humidity impact the unconfined compressive strength of Raw Earth (RE); in 2014, Bui et al. [10] proved that water content alters four key mechanical parameters, and subsequent studies by Gao et al. [11], M. Jiang et al. [4], and Kosiński et al. [12] have further highlighted the importance of moisture and hygrothermal conditions. Collectively, these studies indicate that URE degradation is not purely mechanical, but is affected by coupled interactions between moisture transport, temperature variation, suction evolution, and mechanical loading [8, 10, 13, 14].

Fully coupled THM modeling of URE remains limited, although it is not absent from the literature [13, 14]. Zhang and Nowamooz [13] proposed a theoretical framework for the coupled THM behavior of URE walls subjected to environmental and mechanical loadings, implementing analytical equations within a finite-element numerical environment. And in another study, Zhang and Nowamooz [14] investigated the influence of material type, compaction state, outdoor relative humidity, outdoor temperature, wall geometry, wind speed, cloud cover, radiation, and vertical loading on the THM performance of URE walls. These studies are important because they demonstrate that hydraulic, thermal, and mechanical properties of URE walls are interconnected and can be treated within a coupled theoretical or numerical framework [13, 14].

However, existing THM studies remain mainly physics-based and are generally oriented toward wall-scale indicators such as waterproof capacity, thermal insulation, pushover strength, and horizontal stress limits [13, 14]. Consequently, the localized prediction of continuous damage and stress redistribution fields from environmental and mechanical inputs remains insufficiently explored for modern URE [7, 13, 14].

In parallel, Machine Learning (ML) and DL have become increasingly relevant in civil engineering and materials research because they can serve as surrogate tools for property prediction, structural damage detection, image-based diagnosis, and accelerated evaluation of complex systems [15-17]. In the specific field of RE, however, DL applications remain scarce [7, 18, 19]. Narloch et al. [19] demonstrated the potential of computer vision for RE characterization by using a deep CNN to predict the compressive strength of cement-stabilized RE from scanning electron microscope images. More recently, Waibel et al. [7] proposed a hybrid CNN-LSTM strategy to estimate hygrothermal properties of a RE construction from short-horizon measurements and simulated data. These studies show that DL can reduce reliance on costly and time-intensive characterization procedures, but they do not address coupled environmental degradation, mechanical damage evolution, or spatial stress redistribution in modern URE [7, 19].

Spatial DL architectures, particularly U-Net, offer a promising route for problems where the target response is not a single scalar value but a continuous spatial field [18, 20]. U-Net-based and related segmentation models are now widely used in civil-engineering contexts such as crack detection, semantic segmentation, surface-damage mapping, and infrastructure condition assessment [18, 21-23]. In the specific context of earthen heritage materials, Matich et al. [18] applied U-Net variants with transfer-learning backbones to detect, segment, and assess cracks in historical Tabiya basins. This confirms the potential of U-Net architectures for automated visual assessment of earthen heritage structures, but the task remains post-damage surface segmentation rather than prediction of active mechanical stress states. Therefore, existing U-Net applications related to earthen construction do not yet address THM-driven degradation or continuous stress-field prediction in modern URE.

Accordingly, a clear research gap remains at the intersection of URE mechanics, environmental degradation, FEA stress representation, and spatial DL. Existing studies have separately addressed mechanical characterization, moisture sensitivity, hygrothermal transfer, coupled THM modeling, DL-based property estimation, and visual damage segmentation in RE or earthen heritage materials [5, 7, 8, 10, 14, 18]. Yet, to the best of the authors' knowledge, no previous study has developed a unified computational stress framework that combines THM-informed synthetic data generation, equilibrium-consistent FEA stress targets, with CNN and U-Net-based prediction of both global mechanical responses and continuous spatial damage and stress fields in URE.

The present study addresses this gap by introducing an integrated DL surrogate framework for THM-informed degradation assessment in URE walls. The framework

generates synthetic environmental and mechanical fields, represents each sample through a 5-channel input tensor consisting of temperature, relative humidity, structural texture, initial elastic modulus, and applied strain, and computes corresponding stress responses using a two-dimensional plane-stress finite-element stage. A CNN is then trained to predict global scalar outputs, including the global damage index and reaction-based global FEA stress, while a U-Net is trained to predict continuous spatial damage and FEA-derived stress fields.

The novelty of this work lies in coupling THM-informed image-based data generation with equilibrium-consistent FEA stress targets and spatial DL prediction. Unlike conventional approaches that rely only on destructive testing, isolated scalar mechanical indicators, or repeated finite-element analysis for each new evaluation, the proposed framework provides a proof-of-concept surrogate pathway for inference after training, avoiding repeated execution of the full target-generation pipeline for each network prediction. By focusing on the damage threshold to restricted post-threshold regime of the quasi-brittle response under variable humidity, temperature gradients, stiffness heterogeneity, and applied strain, the study offers a physically informed basis for evaluating environmentally induced degradation in URE. The physical plausibility of the generated trends is further assessed through literature-based experimental and numerical benchmarking against published URE studies.

2. Theoretical Background: Surrogate and Spatial DL Models

2.1. Metamodeling Principle

A metamodel, which can also be called a surrogate model, is a simplified representation of a complex simulation or process using mathematical approximation [24]. The surrogate model can be used to estimate the input-output relationships of the 'black-box' model (the original simulation) where the true relationship is either unknown or computationally too demanding to calculate [25]. By training the metamodel on a limited set of data points from the original model, it creates a functional relationship between input variables x and output $Y(x)$, allowing for 'cheap' and rapid evaluations of system behavior without the need for exhaustive, high-cost simulations (Figures 1 and 2) [26].

A variety of metamodeling approaches exist, including Polynomial Response Surfaces (PRS), Polynomial Chaos Expansions (PCE), Artificial Neural Networks (ANN), Gaussian Process Modeling, and Support Vector Machines (SVM) [25]. The optimal metamodel architecture (i.e., how it will be implemented mathematically) for a given application depends on what the user wants to achieve with the application and the underlying physics the model aims to simulate [26].

The construction of the metamodel is organized into three primary stages [26]:

- Design of Experiments (DoE) to strategically sample the input and maximize information gain.
- Selection of the metamodeling technique (e.g., SVM or ANN), to establish the mathematical framework.
- Model fitting and validation, where numerical optimizers are used to calibrate the model parameters, followed by a validation strategy (e.g., cross-validation) to evaluate the predictive accuracy through statistical metrics (e.g., Mean Squared Error)

Figures 1 and 2, inspired by the study by Negrin et al. [26], illustrate the modeling hierarchy, showing that moving from the real world to metamodels reduces the number of inputs and computational cost at the expense of absolute accuracy and a conceptual overview of the metamodeling process, respectively.

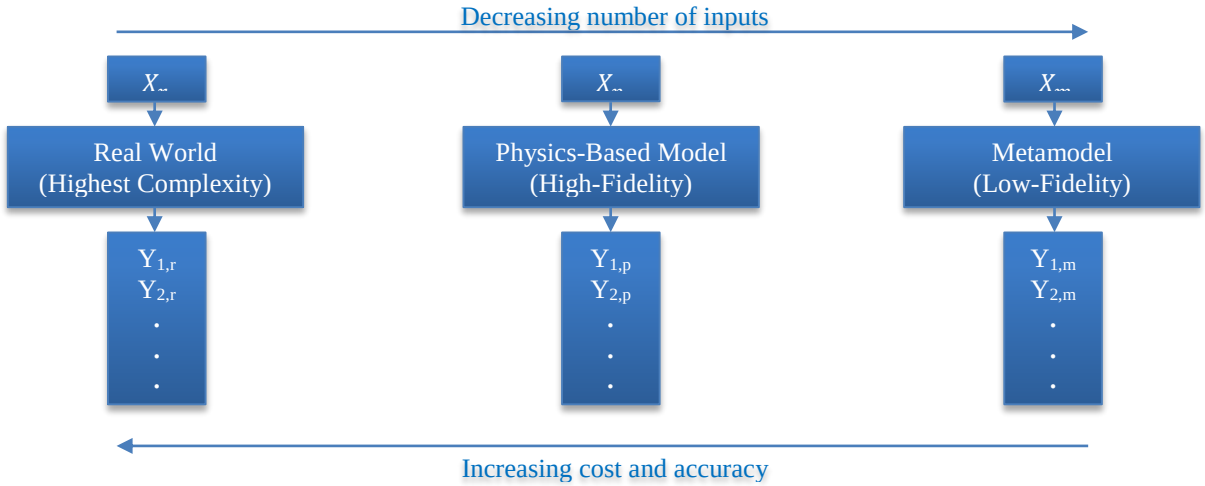

Fig. 1 Hierarchy of modeling approaches illustrating the trade-off between input complexity, computational cost, and predictive accuracy (inspired by [26])

2.2. Convolutional Neural Networks (CNN)

2.2.1. Overview and State-of-the-Art

As a fundamental architecture of DL, especially when it comes to autonomously analyzing and extract spatial patterns from visual imagery [27-29], CNNs draw their design inspiration from the biological concept of the receptive field, which was proposed in Hubel & Wiesel's [30] study of animal visual cortex cells. The widespread adoption of CNNs was initiated by the ImageNet Large Scale Visual Recognition Challenge in 2012. In the challenge, the AlexNet model demonstrated superior performance over existing models at the time, and established CNNs as a central component of computer vision research [31, 32].

Figure 3 places the DL architecture within the larger Artificial Intelligence (AI) hierarchy.

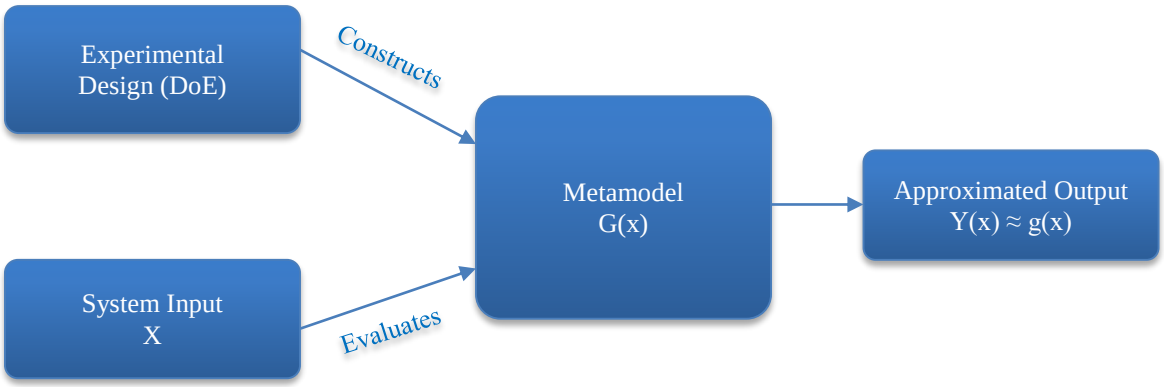

Fig. 2 Schematic of a metamodel $G(x)$ using experimental design (DoE) to approximate the true system response $g(x)$ (Inspired by [26])

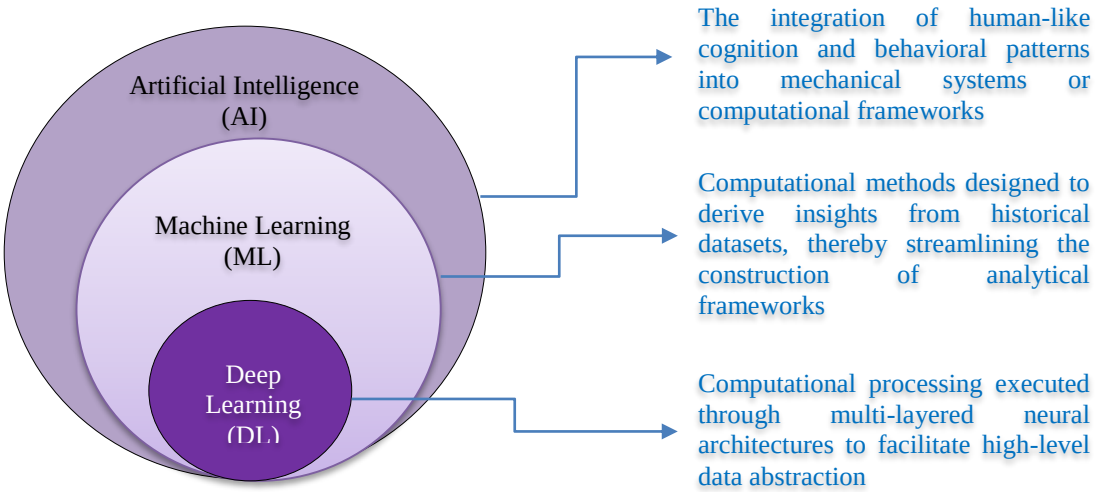

Fig. 3 The structural hierarchy of AI, ML, and DL. Adapted from Sarker [33]

Among other studies, the research by Mann & Kalidindi [34] confirms that CNNs achieve exceptional performance in mapping highly complex and non-linear relationships and that in a wide range of domains. As a matter of fact, it was proved that CNNs achieve far higher accuracy than traditional ML methods when processing large-scale pixel data and have already been deployed in computer vision, natural language processing, various image analysis applications and machine vision scenarios, and serve as a core supporting technology driving the development of the AI field [32, 33]. A primary advantage of this architecture is its ability to circumvent the need for explicit feature engineering; instead, the network implicitly learns to identify critical spatial patterns during the model training process [34]. In recent years, CNNs have catalyzed paradigm shifts across a multitude of disciplines, including image classification, medical imaging, autonomous vehicles, natural language processing, video analytics, generative modeling, environmental monitoring and retail and E-commerce, by leveraging their profound capacity to autonomously extract and learn hierarchical data representations [32].

In the medical field, prior research has developed CNNs into a critical illness diagnosis tool that supports clinicians to quickly identify high-risk lesions [32]; in the transportation

and visual scene understanding, encoder-decoder CNN architectures have been applied to semantic segmentation [35]; CNN-based models have also been used for action recognition and spatiotemporal feature learning [36]; visual similarity in product design [37]; and crop and weed segmentation [38]; these applications illustrate the adaptability of convolutional architectures across diverse image and sequence-based tasks [32].

As this technology integrated across disciplines, a large number of Structural Health Monitoring (SHM) studies based on CNNs have also emerged in the civil engineering field [15] which allowed the detection of structural degradation into a primary focus for image segmentation research [27]: For instance Alcantara and Saito [28] completed automated assessment of post-earthquake structural damage by analyzing absolute acceleration and inter-storey drift within 3D building frames; Gonthina et al. [27] achieved accurate detection and quantification of concrete cracks; Mann and Kalidindi [34] developed a CNN-based modeling of the intricate relationship between a composite's physical properties and its internal microstructure; to maintain a reliability of the predictive model under real-world uncertainties, Zhan et al. [29], investigated the impact of the inherent randomness of physical parameters such as the elastic modulus, on the accuracy of the diagnostic of CNNs used in structural assessment.

Steps and General Workflow

A CNN is composed of three main layers: convolutional layers, pooling (or subsampling) layers, and fully-connected layers. Each of these layers plays a specific role in processing and learning from the input data.

Stage I: The Convolutional Layer (Feature Extraction): The process begins with the convolutional layer, whose primary objective is to identify and analyze the salient features of the input [27]. It performs a linear operation by convolving the input with a learned kernel, also known as a filter (i.e., a small matrix of learnable parameters that slides across the input to detect local patterns and produce feature maps [39]), followed by the application of a pointwise non-linear activation function to the resulting feature map [34]. At this stage, the network leverages weight sharing to detect local receptive fields [40].

- Hierarchical Detection: The initial layers extract low-level features such as edges and simple patterns, whereas deeper layers capture more complex, high-level representations such as shapes and objects [27].
- Mathematical Definition: For a 2D image x and kernel K, the discrete convolution operation, denoted by $*$, at spatial coordinates (u, v) is defined in Equation 1 [39]:

$$S(u,v) = (K * x)(u,v) = \sum_m \sum_n x(u-m, v-n)K(m,n) \quad (1)$$

- Complete Layer Definition: To achieve weight sharing and process the full sequential input, this operation is expanded into the complete convolutional layer defined in Equation 2 [40]:

$$y_j = f\left(\sum_i K_{ij} * x_i + b_j\right) \quad (2)$$

Where y_j denotes the j-th output map for the convolutional layer, K_{ij} denotes the convolutional kernel interaction with the i-th input map x_i, and b_j denotes the bias; furthermore, f denotes the non-linear activation.

- Coarsening: A stride can be introduced to effectively downsample the input, reducing high-dimensional spatial representations into low-dimensional feature maps [34].

Stage II: The Pooling Layer (Dimensional Reduction): Positioned between convolutional layers, the pooling (or subsampling) layer operates as a dimensionality mechanism to effectively down-sample the volume of extracted features [27]. Crucially, this subsampling process introduces spatial invariance, rendering the network robust against small geometric deformations within the input data [27]. In practice, this reduction is achieved through standard Max Pooling or Average Pooling operations, though specific architectural designs may employ Global Average Pooling (GAP) to condense an entire feature map into a single representative value [34, 40].

Stage III: The Fully-Connected Layer (Classification) The final input of the feature extractor is fed into the fully-connected layers, which process each input feature independently. This allows the network to learn complex relationships between the extracted features, but also makes the model more prone to overfitting due to the large number of parameters [34]. These layers generate the final output for classification, often employing a softmax layer at the top to produce probability distributions over the target classes [40]. To visualize these steps, Figure 4 illustrates the foundational architecture of CNN.

2.3. U-Net

2.3.1. Overview and State-of-the-Art

In recent years, the rapid rise of DL and image segmentation technologies has driven transformative changes in visual inspection across numerous fields [41]. In the civil engineering sector, crack detection models built on CNNs have gradually replaced traditional methods, including manual on-site inspections and threshold segmentation [42], and U-Net stands out as a predominant architecture driving this transformation in spatial feature modeling [32]. The U-Net architecture was first proposed by Ronneberger et al. [20] at the Medical Image Computing and Computer-Assisted Intervention (MICCAI) conference in 2015.

Originally created as an image segmentation system for medical images, this architecture design is composed of a symmetrical encoding and decoding system with skip connections to allow for multiple scale feature fusion [41-43]. This architecture has become the standard for defining complex anatomical structures due to its excellent results in detecting brain tumor [44], segmenting cardiac MRIs [45] and analyzing microscopic cells [46].

Beyond its foundational use in biomedicine, U-Net and its variants have rapidly expanded into nearly every field where precise, pixel-wise segmentation is critical. In macro-scale applications, U-Net has been successfully adopted for oceanographic imaging [47], ecology and environmental monitoring [48], precision agriculture [38], and remote sensing [49].

Most notably for engineering disciplines, the architecture has proven highly effective for automated defect segmentation: Tabernik et al. [50] adapted U-Net for surface-defect detection in computer-assisted manufacturing, while Wong et al. [51] successfully detected micro-pores and cracks in X-ray CT scans of additively manufactured components.

Furthermore, it has been widely used in civil engineering, especially in automated visual inspection systems, SHM, material characterization, and infrastructure assessment, due to its superior capacity to detect cracks and structural defects [42]. Recent literature reviews highlight the growing integration of DL, specifically computer vision models, into SHM for crack detection, surface degradation analysis, and precise defect localization.

Until now, DL research in civil engineering has predominantly focused on standard materials like concrete: Mahbub et al. [52] proposed a hand-labeled image dataset to train a U-Net semantic segmentation model that automates the pixel-level detection of concrete surface cracks for SHM.

Recent literature demonstrates that modified U-Net architectures are the state-of-the-art for extracting exact morphological crack data: Hadinata et al. [53] compared U-Net and DeepLabV3+ for concrete-surface crack detection and reported an accuracy of 96.57% for U-Net, while also comparing the obtained performance with previously reported FCN-based approaches.

To address complex background noise on concrete surfaces, researchers are increasingly integrating transformer mechanisms into the segmentation architecture: For instance, Sarhadi et al. [54] proposed an attention-based SWIN U-Net model specifically for concrete crack detection; while Khan et al. [55] adapted a Dense U-Net architecture to assess critical infrastructure, specifically monitoring concrete railway sleepers.

Steps and General Workflow

Building on the general basic CNN operations outlined in the previous section, the U-Net DL network designed for the structural defect segmentation task first adapts its framework from general image classification to dedicated pixel-level segmentation by entirely discarding the fully connected layers corresponding to Stage III in the CNN architecture's workflow. The core logic that enables this network to achieve robust feature extraction and spatial fusion can be broken down into four sequential mechanisms:

The Contracting Path (Encoder Execution): The network repeatedly invokes the mathematical operations of the convolutional block defined in Stage I, paired with non-linear activation and the pooling operations defined in Stage II.

Each round of downsampling halves the input's spatial dimensions and doubles the number of feature channels to extract deep contextual semantics of structural defects. However, this process inevitably loses precise spatial resolution [20]

The Expanding Path (Decoder Execution) : Following the classic foundational framework of Ronneberger et al. [20], the network uses a transposed convolution (up-convolution) to gradually expand the spatial dimensions of the feature map, while halving the number of feature channels accordingly to map the compressed latent space back to the fine spatial geometric dimensions of the original input.

Feature Fusion via Concatenation: Through skip connections, the high-resolution feature maps output by the contraction path are directly concatenated with the upsampling output of the same-layer decoder to compensate for the fine-grained spatial coordinate loss caused by pooling operations. This is how a combination of deep defect semantic information with the precise physical boundary information extracted by the initial layers is achieved, which provides support for high precision pixel-level boundary localization [20, 56].

Final Mask Generation: At the end of the network, we use a 1×1 convolution to generate a final tensor from the fused multi-channel features. The final tensor represents a pixel-level probability map, rather than the probability distribution of target categories for the entire image. The final output is a precise spatial mask representing identified structural defects [20, 56].

The general U-Net architecture shown in Figure 5 demonstrates how the contracting encoder path is symmetrical to the expanding decoder path, and how these paths are connected through skip connections (dashed lines), which combine early high-resolution feature maps with the upsampled outputs.

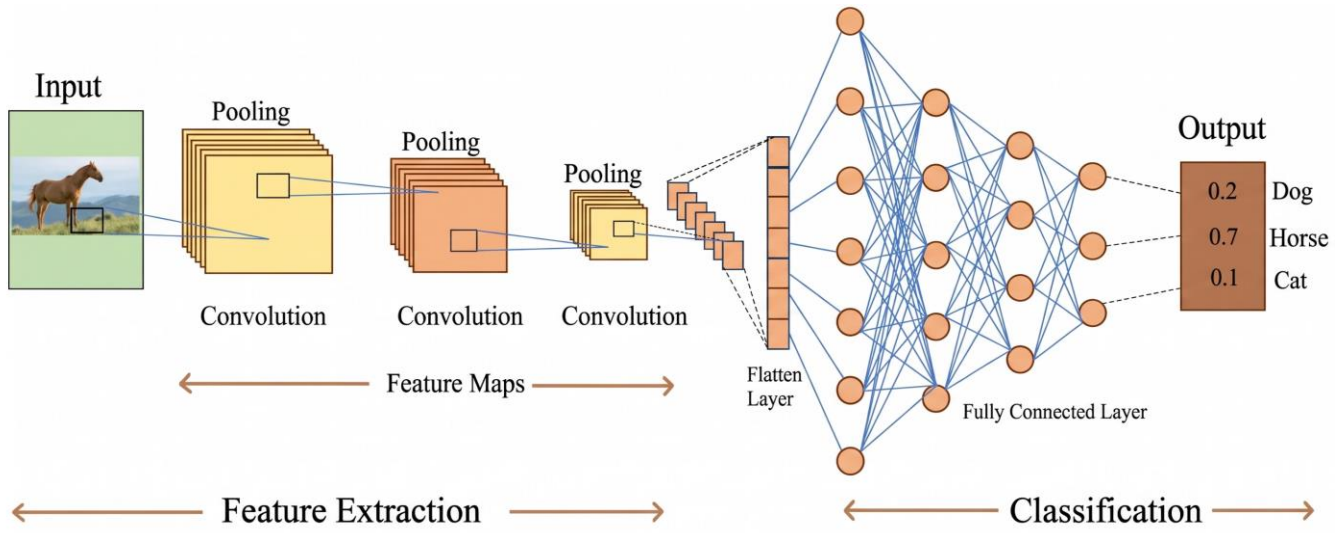

Fig. 4 A fundamental CNN architecture demonstrating the progression from feature extraction to final classification. Adapted from Reza et al. [32], illustrating the foundational network structure originally conceptualized by LeCun et al. [57]

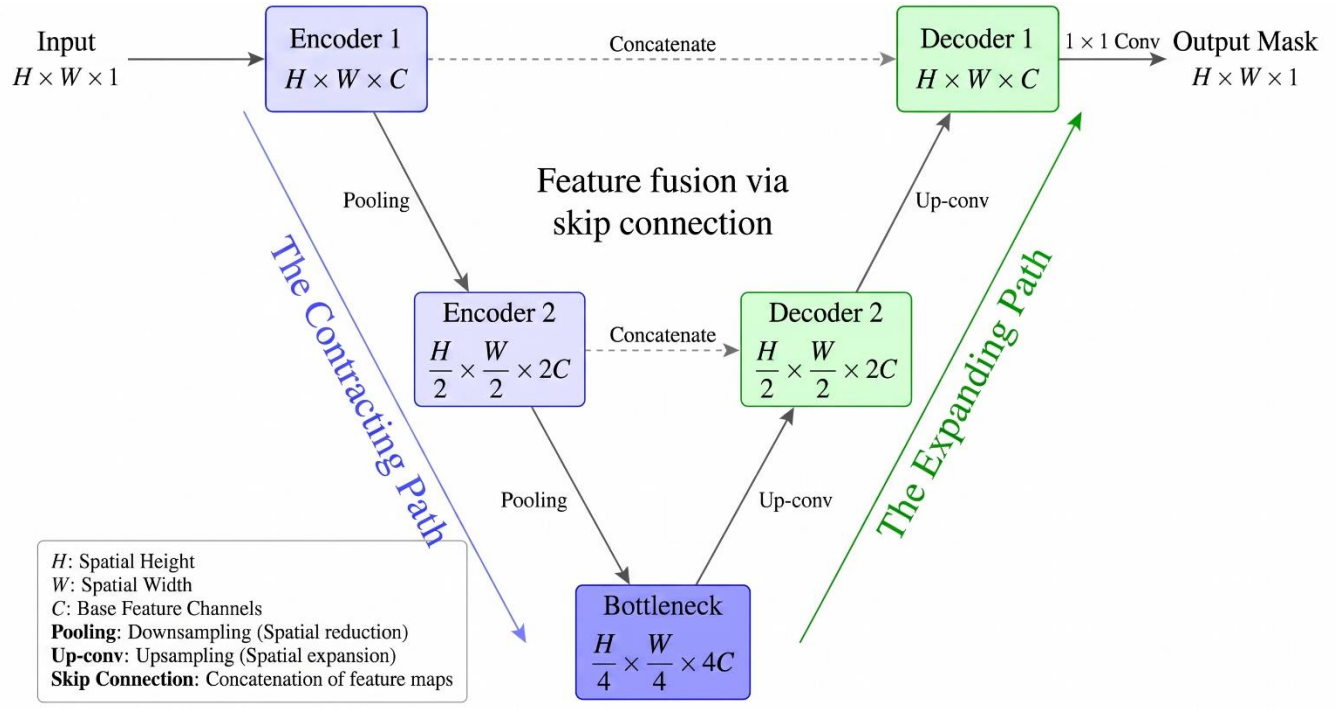

Fig. 5 Generalized U-Net architecture

3. Methodology

3.1. Overall Framework and Computational Environment

The study proposes an integrated DL surrogate framework to evaluate the THM degradation of URE walls. The framework is organized into three computational stages. First, a synthetic data-generation engine produces temperature fields, relative humidity fields, structural texture patterns, material stiffness parameters, and applied strain values for 2,000 URE samples. Second, the generated THM-degraded stiffness fields are used in a two-dimensional plane-stress finite-element stage to compute equilibrium-consistent global and spatial stress targets. Third, two neural-network architectures are trained on the generated dataset: a CNN for global scalar prediction and a U-Net for spatial damage and stress-field prediction. All data generation, finite-element target computation, and neural-network training procedures were implemented in Python within the Google Colab environment. The CNN receives the 5-channel THM-mechanical input tensor and predicts the global damage index and global FEA stress. The U-Net receives the same input tensor and predicts the corresponding spatial damage map and normalized FEA-derived stress field.

3.2. Material Assumptions and Governing Equations

URE is modeled as a heterogeneous, quasi-brittle material subjected to compressive stress. The mechanical degradation is modeled within the damage-threshold to restricted post-threshold regime of the stress-strain curve.

The theoretical foundation of the synthetic data engine relies on three primary interacting mechanics:

- Environmental Coupling (THM Attenuation): Designed to model environmental degradation by using a localized THM attenuation factor, $\Pi_{THM}(x, y)$, that aims to reduce material performance based on the local relative humidity field and the spatial temperature gradient, therefore representing phenomenological environmental weakening motivated by moisture-suction-strength coupling and thermal-gradient effects. The supporting unsaturated earthen materials related studies include those by Jaquin et al. [8], Bui et al. [10], Beckett and Augarde [9], and Jiang et al. [58].
- Constitutive Global Damage: Used to simulate the mechanical degradation, and is achieved by adopting the continuum damage framework proposed by Mazars and Pijaudier-Cabot' [59]. To simulate post-threshold micro-structural degradation, the applied strain ($\varepsilon_{applied}$) is randomly sampled just beyond the URE elastic threshold of $\varepsilon_{d0} = 0.005$, and the scalar damage variable (D) is computed using modified Mazars and Pijaudier-Cabot' parameters (Ac=0.8, Bc=350.0). This setup avoids sudden material collapse and maintains interpretable damage development in URE.
- Material Heterogeneity and Stress Target Preparation: The heterogeneous, compacted nature of URE is represented using a Gaussian random field to simulate spatial variability in compaction, supported by the geotechnical random-field modeling principles of Fenton and Griffiths [60] and Vanmarcke [61]. The resulting compaction field modifies the local stiffness distribution and is combined with the initial elastic modulus, THM attenuation factor, and damage-dependent stiffness reduction.
  The latter follows the general continuum-damage principle whereby increasing damage progressively reduces the effective material stiffness, consistent with the formulations described by Lemaitre [62] and Mazars and Pijaudier-Cabot [59]. To ensure stable neural network optimization, a normalization using a 15 MPa reference stress is applied to transform the spatial stress field.

The main assumptions and target-generation steps are summarized in the following subsections.

3.3. Internal Synthetic Data Pipeline (Inputs and Outputs)

To train the predictive architectures, the generation engine continuously randomizes the material texture, initial elastic modulus, and environmental boundaries.

- The Input Tensor: For every sample, the framework generates a 5-channel tensor composed of: (i) the normalized temperature field, (ii) the normalized relative humidity field, (iii) the grayscale structural texture and compaction-heterogeneity field, (iv) a spatially constant normalized initial elastic modulus map, and (v) a spatially constant normalized applied strain map. Smooth Gaussian random fields for temperature and relative humidity have been independently min-max normalized to the interval [0,1]. In the current synthetic framework, there is no prescription of the dimensional temperature range in °C or relative humidity range in %RH. Therefore, the channels represent relative spatial environmental intensity, and not calibrated physical measurements.
- The Output Targets: he dataset has two types of output targets. The first type includes global scalar targets that will be used to train the CNN: the global damage index D and the normalized reaction-based global FEA stress. The physical global stress in MPa is kept for interpretation and reporting purposes. The second type includes spatial targets that will be used to train the U-Net: the localized damage map and the normalized FEA-derived stress field. The normalized stress field is used to ensure stability during the process of optimizing the neural network. Stress errors from the normalized stress field can then be transformed into MPa to interpret the results.

3.4. Equilibrium-based FEA Stress Target Generation

In order to produce consistent mechanical stress targets, the THM-degraded stiffness fields created during the synthetic data stage were transferred to a 2D finite-element stress computation stage. The URE wall domain was modeled as a plane stress domain with four-node quadrilateral elements. Each element had its own local elastic stiffness based upon the initial elastic modulus, compaction-heterogeneity field, THM attenuation factor, and damage-dependent stiffness reduction.

For each generated sample, a vertical compressive displacement corresponding to the sampled applied strain was imposed along the top boundary of the domain. The bottom boundary was restrained in the vertical direction, while one bottom corner was additionally restrained in the horizontal direction to eliminate rigid-body motion. The lateral boundaries were left free. The finite-element system was assembled and solved to enforce static mechanical equilibrium. After solving for the displacement field, the local strain and stress tensors were recovered at the element level using the plane-stress constitutive relationship.

The spatial FEA stress map was created by extracting the vertical stress component, while the global FEA stress response was calculated using the reaction forces at the loaded boundary. The FEA stress map was stored in two

forms. The first form corresponds to the physical vertical stress field expressed in MPa. The second form corresponds to a normalized stress field obtained by dividing the physical stress values by a reference stress of 15 MPa. The normalized stress maps were used for U-Net training to improve numerical stability, while the physical MPa values were retained for quantitative interpretation of prediction errors.

This finite-element stage was used to generate mechanically consistent global and spatial stress targets. The neural networks were subsequently trained as surrogate models to approximate the relationship between the 5-channel THM-mechanical input tensor and the corresponding global or spatial degradation responses.

The FEA was solved on a 56×56 four-node quadrilateral mesh using four damage-update iterations, a damage-relaxation factor of 0.65, a maximum local damage of 0.95, a residual stiffness factor of 0.05, and a minimum elastic modulus of 5 MPa; the resulting fields were subsequently interpolated to $224x224$ for DL training. At each damage-update iteration, the effective local modulus was computed as $E_{eff} = \max[5\ MPa, E_{base} \max(0.05, 1 - D_{total})]$, thereby enforcing both the residual-stiffness factor and the minimum-modulus bound.

3.5. DL Architectures and Training Configuration

This study uses the generated THM-FEA dataset to train two complementary neural-network architectures. The CNN is used as a global regression model to predict two scalar quantities: the global damage index D and the reaction-based global FEA stress. The U-Net is used as an image-to-image spatial prediction model to estimate the localized damage map and the normalized FEA-derived stress field.

The dataset contains 2,000 samples and was divided into 1500 training samples, 300 validation samples, and 200 independent test samples, corresponding to a 75%/15%/10% split. The validation subset was used during training for model selection and early stopping, while the independent test subset was reserved for the final reported performance metrics. Both architectures were trained using the same 5-channel THM-mechanical input tensor composed of temperature, relative humidity, structural texture, initial elastic modulus, and applied strain. The implemented CNN used five 3x3 convolutional blocks with 32, 64, 128, 256, and 256 filters, followed by global average pooling and dense layers of 256, 128, and 64 units with 0.20 dropout. The U-Net used encoder depths of 32, 64, and 128 filters and decoder depths of 64 and 32, with skip concatenation and separate 1x1 sigmoid output heads. Both models used a batch size of 16; Adam learning rates were 3×10^{-4} for the CNN and 1×10^{-3} for the U-Net, with early stopping patience of 18.

Figure 6 illustrates the overall workflow of the THM-informed synthetic data generation, equilibrium-based FEA stress target computation, and CNN/U-Net training pipeline.

Table 1. DL training hyperparameters and configuration

Parameter	Configuration
Dataset Size	2,000 synthetic THM-FEA samples
Input Tensor	5 Channels: Temperature, Relative Humidity, Structural Texture, Initial Elastic Modulus, Applied Strain
Dataset Split	1500 training / 300 validation / 200 test samples
Equivalent Split	75% Training / 15% Validation / 10% Test
Maximum Epochs	100 (with Early Stopping)
Optimizer	Adam
CNN Task	Global Scalar Regression
CNN Outputs	Global Damage Index D; Global FEA Stress
CNN Loss Function	Mean Squared Error (MSE)
CNN Training Metric	Mean Absolute Error (MAE)
CNN Evaluation Metrics	Coefficient of Determination (R^2), Root Mean Square Error (RMSE), MAE
U-Net Task	Spatial Image-To-Image Prediction
U-Net Output	Localized Damage Map; Normalized FEA Stress Field
U-Net Loss Functions	Combined Structural Similarity Index Measure (SSIM)-MAE Loss
U-Net Evaluation Metrics	SSIM, RMSE, MAE
Stress Normalization	Global and Spatial FEA Stress Targets Normalized by 15 MPa for Training; Errors Converted back to MPa for Interpretation.

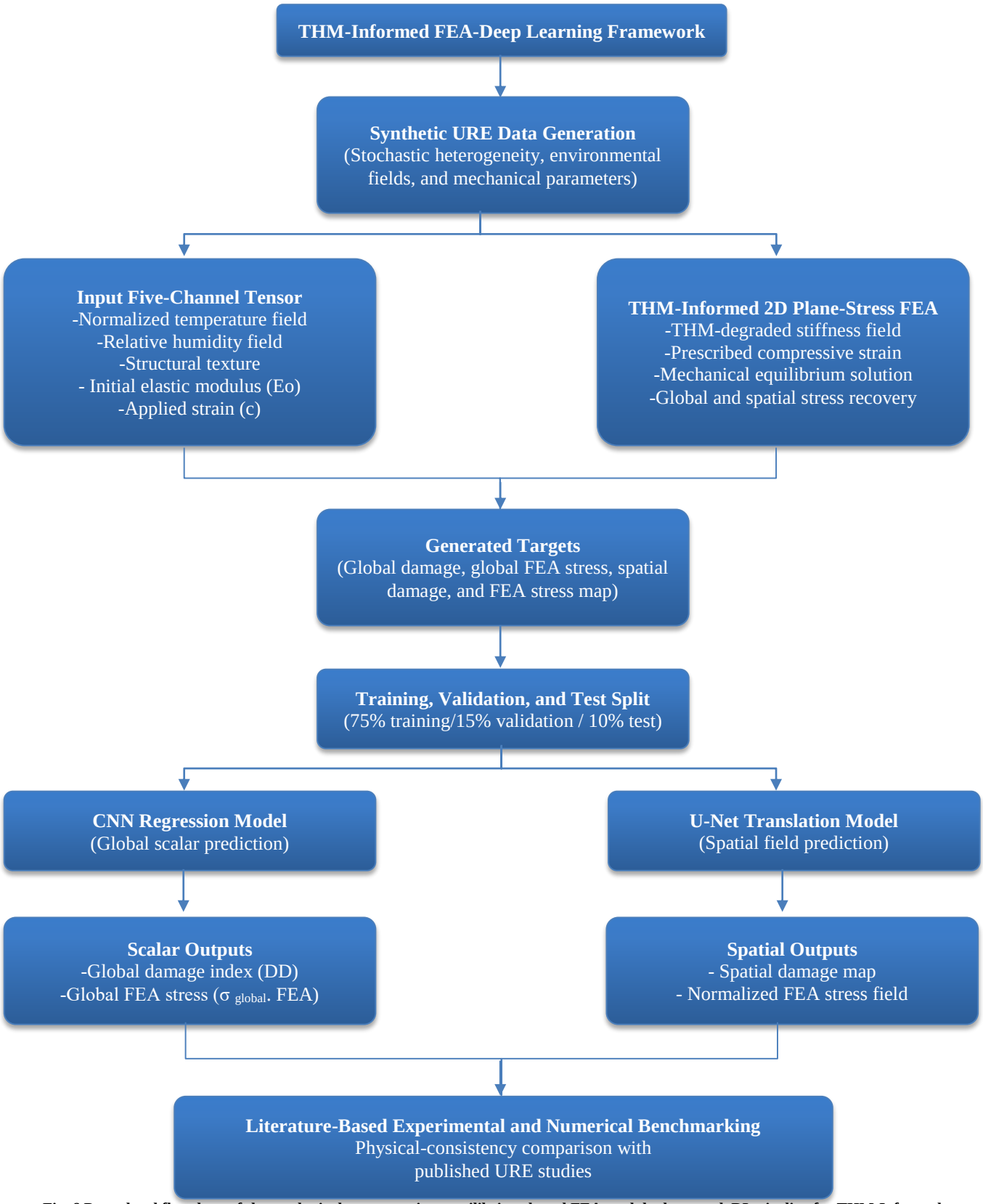

Fig. 6 Procedural flowchart of the synthetic data generation, equilibrium-based FEA, and dual-network DL pipeline for THM-Informed degradation assessment in URE structures

4. Results

4.1. Dataset Characteristics and Visualized THM Scenarios

The results reported in this section correspond to the final 5-channel THM-FEA dataset, in which each synthetic sample includes temperature, relative humidity, structural texture, initial elastic modulus, and applied strain as input information, together with global damage, global FEA stress, spatial damage, and normalized FEA stress targets.

To train DL architectures without relying on resource-intensive physical compression experiments, a synthetic dataset of 2,000 unique URE samples was generated dynamically in memory. The synthetic model represents compressive loading of heterogeneous URE geometries. To capture real-world material heterogeneity and the significant stiffness variations inherent to earthen elements, the framework initialized the reference initial elastic modulus (E_0) stochastically. Rather than using a single deterministic baseline, E_0 is sampled from a normal distribution with a mean of $400\ MPa$ and a standard deviation of $150\ MPa$ and bounded between 100 MPa and 800 MPa, reflecting a low-to-moderate stiffness range compatible with the variability for URE materials [2].

This study develops a procedural degradation and crack-morphology model for URE walls under the assumption that degradation occurs in areas of environmental weakness. To replicate this mechanism, this study generates independent two-dimensional Gaussian random fields for the normalized relative humidity field $H(x,y)$, and the normalized temperature field $T(x,y)$, producing a spatially continuous environmental distribution rather than isolated random values. This approach differs from the discrete random assignment method commonly used in traditional numerical simulations, thereby accurately simulating the gradual change characteristics of local environments that real wall surfaces are exposed to. The humidity field corresponds to localized zones across the surface that accumulate moisture and are prone to dampness, while the temperature field reflects the spatial thermal variation of the wall. Next, this study introduces a local THM attenuation factor that acts as a phenomenological degradation factor. $\Pi_{THM}(x,y)$, to integrate the two types of environmental fields into the mechanical response module.

The physical basis for this attenuation factor is supported by previous experimental and numerical studies on RE and unsaturated earthen materials. Jaquin et al. [8] showed that URE may be interpreted as an unsaturated compacted soil and that matric suction contributes significantly to its apparent cohesion and strength. In their study, strength increased as water content decreased, which confirms that suction-related mechanisms are central to the mechanical resistance of URE. Bui et al. [10] further confirmed that moisture content and suction strongly influence the compressive strength and elastic modulus of RE. Their results showed that strength decreases as moisture content increases, particularly beyond the near-dry range, and their microscopic interpretation attributed this weakening to both the reduction of suction and the weakening of inter-particle cohesion in the clay fraction.

The effect of climate factors is also applicable to the proposed degradation model. Beckett and Augarde [9] investigated the effect of relative humidity and temperature on the Unconfined Compressive Strength (UCS) of RE. Their research considers RE as an extremely unsaturated soil and demonstrates that changes in humidity and temperature alter the suction regime of the soil, thus altering the UCS. Therefore, environmental humidity and temperature can be considered as variables that affect the synthetic degradation framework. Additionally, Jiang et al. [58] examined the hygrothermal properties of RE walls and developed a coupled heat and moisture transfer model. Their model illustrates that temperature gradients contribute to moisture transport via their effects on vapor pressure gradients and capillary pressure gradients. Therefore, while the attenuation function used within this study is not directly derived from the findings of these studies, its structure is physically motivated by documented moisture-suction-strength coupling and by the role of temperature gradients in coupled heat and moisture redistribution in RE walls. The local THM attenuation factor is defined in Equation 3:

$$\Pi_{THM}(x,y) = \exp\big(-\beta \cdot H(x,y)\big) \cdot (1.0 - \gamma \cdot \| \nabla T(x,y) \|) \tag{3}$$

Where $\Pi_{THM}(x,y)$ is the local degradation or performance factor assigned to each spatial position of the URE geometry. A value close to 1 indicates limited environmental degradation, while lower values indicate stronger local weakening.

The first component of the equation is the moisture attenuation term $\exp\big(-\beta \cdot H(x,y)\big)$ in which β is the moisture-sensitivity coefficient. As $H(x,y)$ increases, the exponential term decreases. This behavior represents the progressive loss of mechanical performance caused by moisture ingress, reduction of matric suction, and weakening of clay-related inter-particle cohesion. The exponential form was selected because it provides a smooth, nonlinear, and strictly decreasing degradation function. It is not claimed here as a universal constitutive law for URE, but as a phenomenological representation consistent with the nonlinear moisture sensitivity observed experimentally in RE. The second component is the thermal-gradient penalty term $1.0 - \gamma \cdot \| \nabla T(x,y) \|$ in which $\| \nabla T(x,y) \|$ represents the magnitude of the local spatial temperature gradient, and γ is the thermal-gradient sensitivity coefficient. This term reduces the local performance factor in regions where temperature varies sharply over space. The physical motivation is that temperature gradients can contribute to

coupled hygrothermal imbalance by influencing vapor pressure gradients, capillary pressure gradients, and moisture redistribution within porous earthen walls. The term is therefore used as a simplified penalty for local thermal-gradient effects rather than as a direct mechanical damage law.

The coefficients β and γ were defined as scenario-control parameters rather than calibrated material constants. Since both $H(x,y)$ and $||\nabla T(x,y)||$ were normalized between 0 and 1, the selected values were chosen to produce visible but bounded degradation effects. A value of $\beta = 1.5$ was used for moisture-sensitive cases because it reduces the moisture attenuation term from 1.0 under dry conditions to $\exp(-1.5) \approx 0.22$ under the most humid normalized condition. This provides a strong degradation contrast, consistent with the dominant role of moisture and suction loss in URE weakening. A lower value of $\gamma = 0.4$ was used for thermal-gradient effects because the thermal contribution is treated as secondary; it reduces the thermal factor from 1.0 to 0.6 under the maximum normalized temperature gradient, avoiding excessive or negative degradation. Thus, β was assigned a higher value than γ to reflect the stronger experimental evidence for moisture/suction-driven strength loss in URE, while γ was kept moderate to represent thermal-gradient effects without allowing them to dominate the response. The values and interpretation of the coefficients β and γ for each scenario are summarized in Table 2.

4.2. Global Damage Formulation and Scenario Coefficients

To simulate the post-threshold micro-structural degradation under compression, each synthetic URE specimen is subjected to a global compressive strain ranging from the damage threshold to the restricted post-threshold response. The elastic damage threshold is fixed at $\varepsilon_{d0} = 0.005$, corresponding to 0.5% strain [63-66]. The applied strain is then randomly sampled using a uniform distribution according to $\varepsilon_{applied} \sim U(0.005, 0.009)$, corresponding to 0.5%–0.9% strain. This range spans the damage threshold and a restricted post-threshold strain regime while avoiding the asymptotic severe-damage state of the constitutive law.

The accumulation of global damage is quantified using an analytical instantiation of Mazars' continuum damage framework [59]. The scalar damage variable D is bounded between 0 and 1. Damage is set to zero at or below the threshold strain ε_{d0} and evolves progressively once the applied strain exceeds this threshold, as defined in Equation 4.

In the present implementation, the scalar global damage D is governed solely by the applied strain $\varepsilon_{applied}$ through Equation 4. The temperature, relative humidity, structural texture, and initial elastic modulus do not directly modify this scalar; their influence is introduced through the spatial THM attenuation, heterogeneous damage distribution, local stiffness degradation, and subsequent FEA stress response. This distinction separates the constitutive scalar damage indicator from the spatially varying THM-informed outputs of the framework.

In this formulation, ε_{d0} defines the strain level at which damage begins to evolve. The parameter Ac controls the shape and upper progression of the post-elastic damage curve, while Bc controls the rate of damage growth after the elastic threshold is exceeded.

In classical Mazars-type models developed for concrete, these parameters are usually identified from uniaxial tensile and compressive tests [59]. For concrete applications, typical values reported in model documentation place Ac generally between 1 and 2, and Bc between 1000 and 2000, while one sample concrete parameter set gives $Ac = 1.4$ and $Bc = 1850$ [59].

However, these concrete-based values are not directly transferable to URE, and due to the absence of empirical calibration data in current RE literature, Ac and Bc were not treated as experimentally fitted constants for a specific URE mixture. Instead, they were selected as phenomenological shape parameters aiming to regulate post-threshold damage kinetics within the synthetic data generation pipeline. In the present model, Ac is set to 0.8 and Bc to 350.0. These values are lower than typical concrete-oriented Mazars and Pijaudier-Cabot's parameters, which avoids an excessively abrupt collapse-type response within the selected post-threshold strain range of 0.5%–0.9%. The chosen values allow damage to increase rapidly after the elastic threshold while still maintaining a gradual and visually interpretable development of cracking.

Within the adopted strain range of $0.5\% - 0.9\%$, Equation 4 produces scalar damage values from $D = 0$ at the threshold to a theoretical maximum of approximately $D = 0.692$ at 0.9% strain. Values approaching $D = 1$ refer to the broader asymptotic range of the constitutive formulation and are not reached by the samples generated in the present study. Accordingly, values around $D = 0.5 - 0.7$ are interpreted as moderate-to-high damage states within the sampled post-threshold regime rather than as initial damage. The corresponding prior spatial damage field was constructed as $D_{prior}(x,y) = clip\left[\left(1 - \Pi_{THM}(x,y)\right) + M_c(x,y)D, 0,1\right]$, where $M_c(x,y)$ denotes the procedurally generated crack mask. A principal vertical crack was generated preferentially in environmentally weakened regions, while an additional diagonal branch could occur for $D > 0.5$. These features represent procedural damage morphology rather than explicit fracture-propagation mechanics.

Table 2. Sensitivity coefficients adopted for the humidity-only, temperature-only, and coupled THM degradation scenarios

Scenario	β	γ	Interpretation
Humidity-only	1.5	0	Strong moisture-driven weakening; thermal effect disabled
Temperature-only	0	0.4	Moderate thermal-gradient penalty; moisture effect disabled
Coupled THM	1.5	0.4	Combined moisture-dominant and thermal-gradient degradation

$$D = \begin{cases} 0 & \varepsilon_{applied} \le \varepsilon_{d0} \\ \max\left(0, min\left(1, 1 - \dfrac{\varepsilon_{d0}(1-Ac)}{\varepsilon_{applied}} - Ac\ exp\left[-Bc\left(\varepsilon_{applied} - \varepsilon_{d0}\right)\right]\right)\right) & \varepsilon_{applied} > \varepsilon_{d0} \end{cases} \quad (4)$$

The resulting D-value acts as the main control parameter for the subsequent visual and mechanical generation process. It governs the severity of cracking by influencing the probability of crack branching, the aperture of cracks, and the density of detached micro-voids. Low values of D correspond to limited early damage, whereas values approaching 1 represent severe degradation and more developed cracking patterns.

4.3. FEA-based Stress Target Analysis

The mechanical response of the generated URE samples was characterized by transferring the THM-degraded material fields into a two-dimensional plane stress finite element model. The local stiffness distribution included the initial elastic modulus, compaction heterogeneities, environmental attenuations, and damage-dependent degradations.

Each sample had its prescribed compressive strain applied through the upper boundary; however, it was also subjected to appropriate displacement constraints to avoid rigid-body motion. From the resulting displacement fields, the local stress distributions could be recovered, providing an equilibrium-consistent vertical stress map for each synthetic configuration.

The FEA was completed for all 2,000 samples. The variation in the resulting global FEA stress response was large across the three environmental scenarios. Of the environmental scenarios, the temperature-only cases exhibited the highest mean global stress, equal to 0.848 MPa, with values ranging from 0.150 to 2.428 MPa. While the humidity-only cases showed a lower mean global stress of 0.326 MPa, with values between 0.066 and 1.107 MPa, whereas the coupled THM cases produced the lowest mean response of 0.265 MPa, with values ranging from 0.053 to 1.007 MPa.

These results indicate a stronger reduction in mechanical response when moisture-related degradation is activated, particularly when humidity and thermal effects act simultaneously. For DL, the FEA stress responses were normalized using a reference value of 15 MPa. The normalized global FEA stress was used as the CNN stress target, while the normalized vertical FEA stress field was used as the U-Net spatial stress target. The corresponding physical values were retained in MPa for quantitative interpretation and reporting of prediction errors.

4.4. Network Integration and Dataset Visualization

To bridge the synthetic generation pipeline with the DL architectures, the dataset was explicitly formatted for two complementary predictive tasks. Both architectures utilize the identical 5-channel THM-mechanical input tensor, but they predict responses at different scales. The CNN performs global scalar regression and predicts the global damage index D and the reaction-based global FEA stress $\sigma_{global,FEA}$. The U-Net performs spatial field prediction and predicts the localized damage map and the normalized FEA-derived vertical stress field. Thus, the CNN represents sample-level mechanical responses, whereas the U-Net represents the spatial distributions of damage and stress.

Figures 7 and 8 illustrate representative examples using the same synthetic THM-FEA pipeline across the three isolated and coupled environmental scenarios. Figure 7 illustrates the generated temperature field, humidity field, and a 3-channel visual superposition of the input data, while the complete neural network input is represented by the 5-channel THM-mechanical tensor, whereas Figure 8 presents the corresponding spatial targets and damaged structural texture, including the spatial damage map, normalized vertical FEA stress field, and damaged texture.

Finally, an excerpt of the dataset metadata is provided in Table 3 to illustrate the ground-truth scalar targets used for CNN training. And it is important to note that across all isolated scenarios (e.g., Temperature-Only), both environmental fields are continuously generated for all scenarios, while the isolation of the physical phenomena is enforced mathematically within the physics engine by zeroing the respective sensitivity coefficients (β or γ), so that the inactive environmental field does not contribute to the corresponding THM attenuation term. It should be noted that β, γ, and the scenario label are not provided explicitly to the neural networks. These coefficients operate upstream within the synthetic generation engine, where they determine how the generated temperature and humidity fields contribute to THM attenuation and consequently affect the degraded

structural state and FEA-derived response targets. The scenario-wise results, therefore represent evaluation on subsets generated under different physical coefficient settings rather than explicit scenario classification by the networks. To assess the possible influence of crack morphology already present in the structural texture channel, a test-time sensitivity analysis was performed on the independent test subset by spatially neutralizing the structural texture channel while retaining the other four inputs unchanged. The overall spatial-damage SSIM decreased from 0.8551 to 0.7719, while the MAE increased from 0.1174 to 0.1273 and the RMSE from 0.1650 to 0.1795.

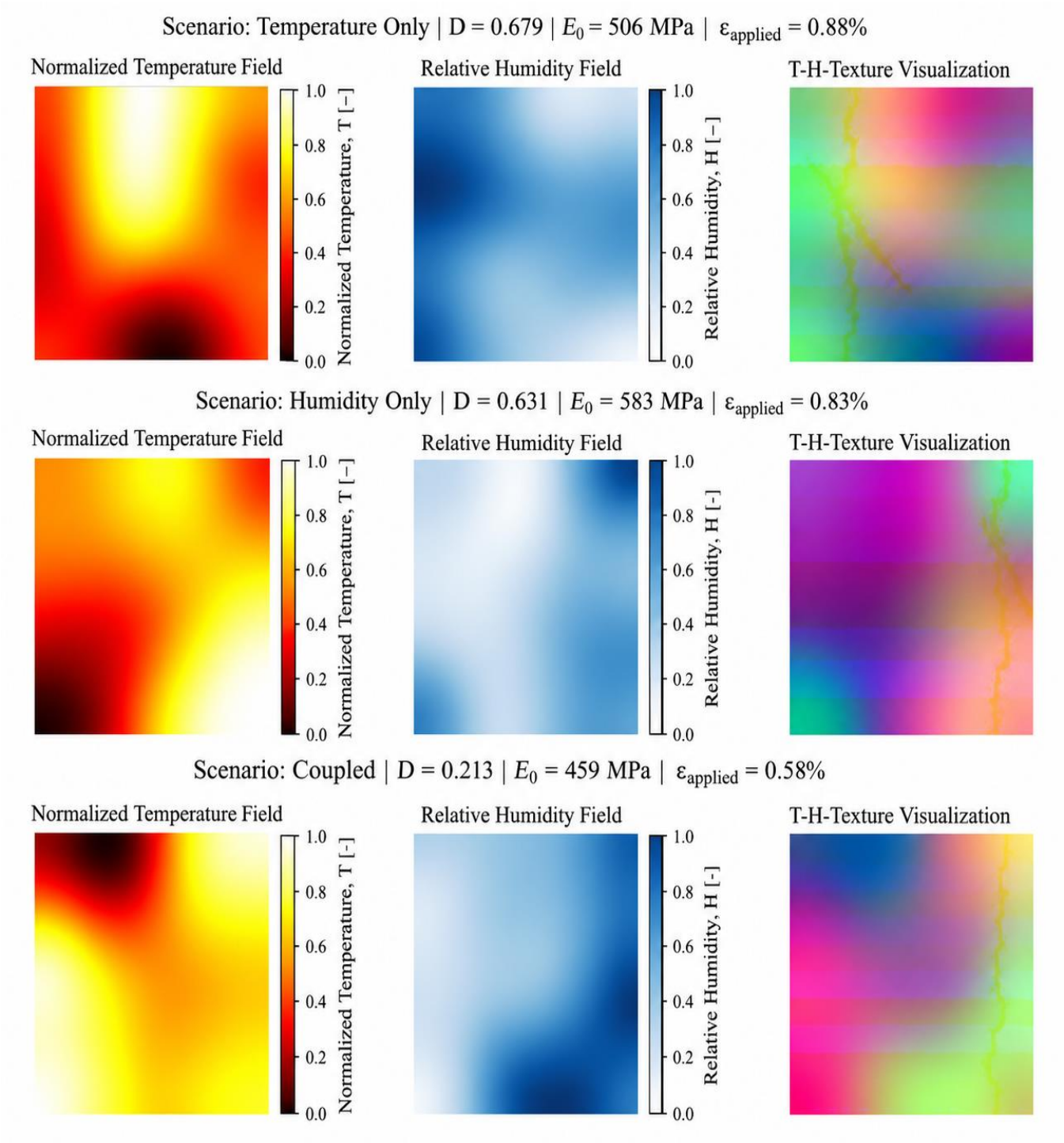

Fig. 7 Representative temperature, relative-humidity, and T–H–texture visualizations for the three environmental scenarios; the Neural-Network input is the complete 5-channel tensor

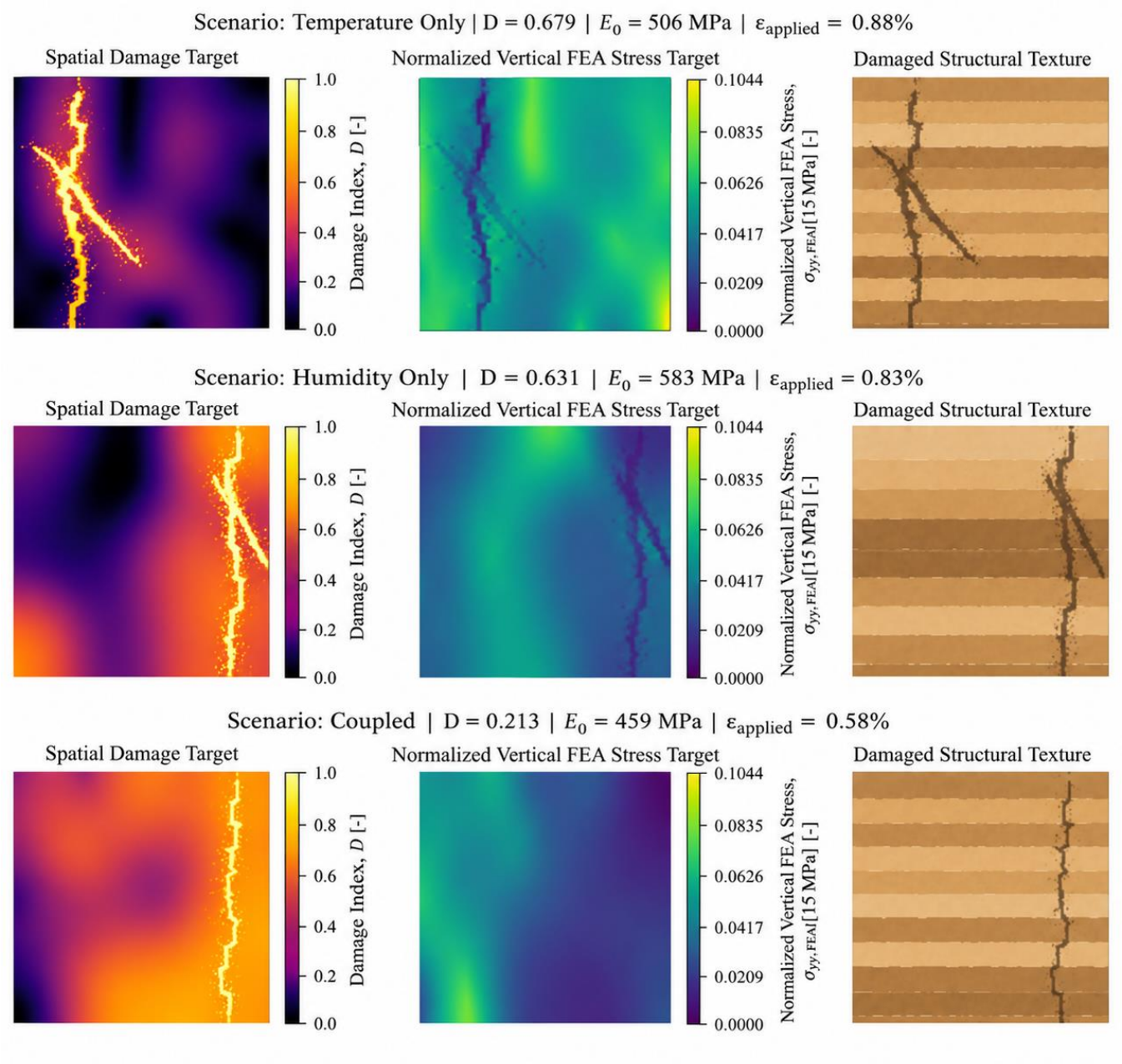

Fig. 8 Representative spatial damage targets, normalized vertical FEA stress targets, and damaged textures for the three environmental scenarios

Table 3. Excerpt from the generated metadata file used for CNN scalar training

Scenario	Global Damage (D)	Initial Elastic Modulus E_0 (MPa)	Applied Strain $\varepsilon_{applied}$ (%)	Global FEA Stress $\sigma_{global,FEA}$ (MPa)
Humidity Only	0.3994	407.79	0.6643	0.2596
Humidity Only	0.5213	425.22	0.7413	0.3082
Humidity Only	0.4114	300.37	0.6711	0.1965
Humidity Only	0.3223	451.62	0.6244	0.3015
Temperature Only	0.5337	326.77	0.7504	0.6895
Temperature Only	0.3995	240.56	0.6644	0.5354
Temperature Only	0.5239	478.98	0.7432	0.8798
Temperature Only	0.1875	385.30	0.5657	0.8042
Coupled THM	0.6694	382.32	0.8738	0.2331

Coupled THM	0.2652	294.30	0.5981	0.1809
Coupled THM	0.5396	208.76	0.7549	0.1038
Coupled THM	0.4212	342.77	0.6767	0.2006
Coupled THM	0.1106	351.99	0.5369	0.5174

4.5. CNN Predictive Performance: Global Scalar Regression

To evaluate the CNN for global scalar prediction, the model was trained using the 5-channel THM-mechanical input tensor to predict the global damage index (D) and normalized global FEA stress ($\sigma_{global,FEA}$). Training was performed for a maximum of 100 epochs with an early stopping mechanism utilizing MSE as the primary loss function for both outputs, while MAE was monitored as a training metric. Because the scalar global damage target D is analytically prescribed from the applied strain through Equation 4, a strain-only analytical baseline was additionally evaluated on the same independent test subset used for CNN assessment. The baseline reconstructed D directly from the applied-strain channel using Equation 4 and achieved $R^2 = 0.999999976$, $MAE = 2.66 \times 10^{-5}$, and $RMSE = 3.03 \times 10^{-5}$. By comparison, the 5-channel CNN achieved $R^2 = 0.995254$, $MAE = 0.011099$, and $RMSE = 0.013392$. The near-exact analytical baseline confirms that global D is fundamentally a strain-defined constitutive target in the present synthetic framework. Therefore, the CNN damage result should be interpreted as successful recovery of this prescribed relationship rather than evidence that the scalar D independently depends on all five input channels.

The baseline results are summarized in Table 4. The final predictive accuracy of the architecture was subsequently evaluated on the independent test subset using R^2, MAE, and RMSE. The training history and scenario-specific regression results for both the global damage index (D) and global FEA stress ($\sigma_{global,FEA}$), and the corresponding test metrics are presented, respectively, in Figures 9-11 and Table 5.

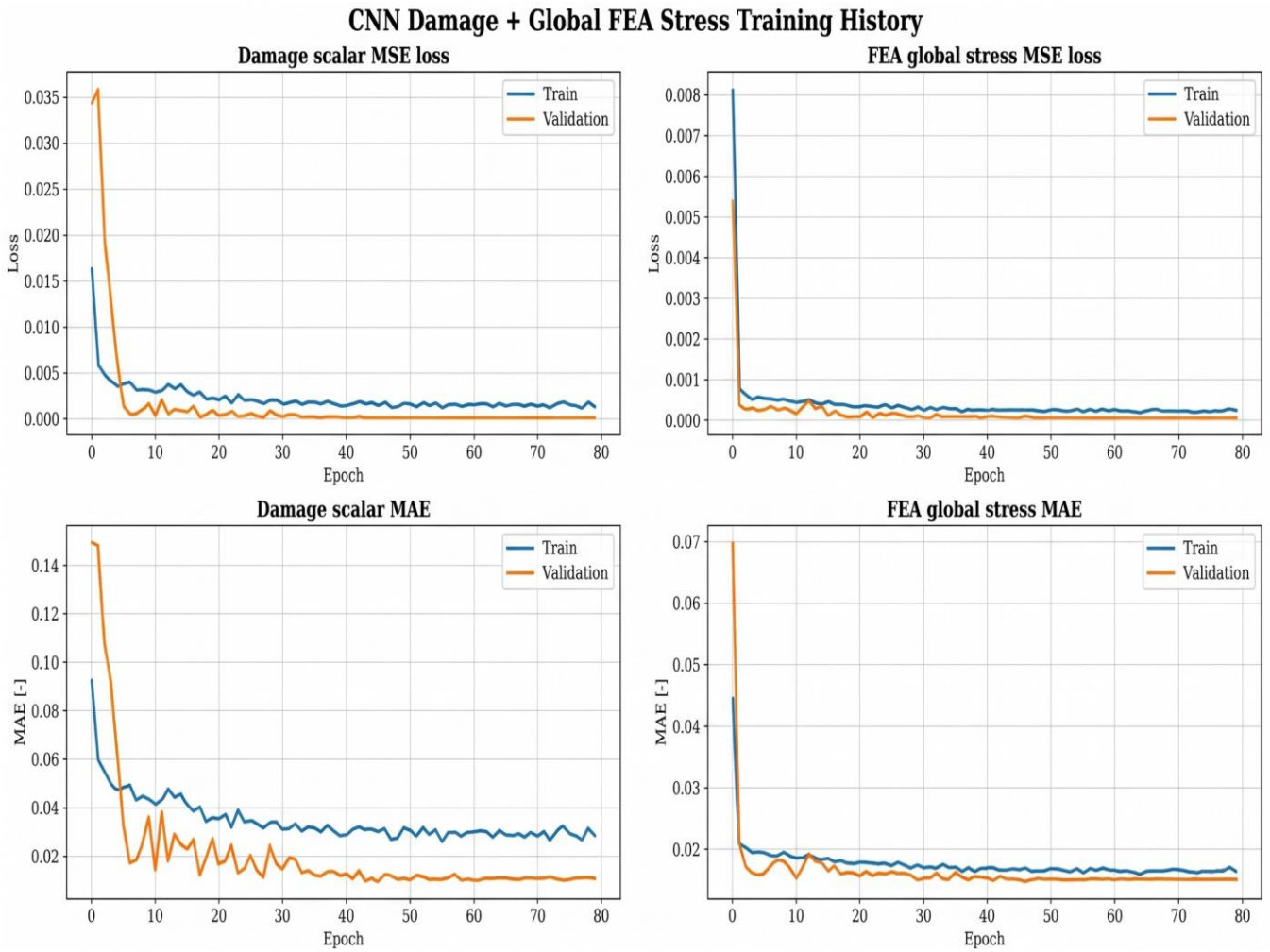

Fig. 9 Training history of the CNN for global damage and global FEA stress prediction, showing MSE loss and MAE across training epochs

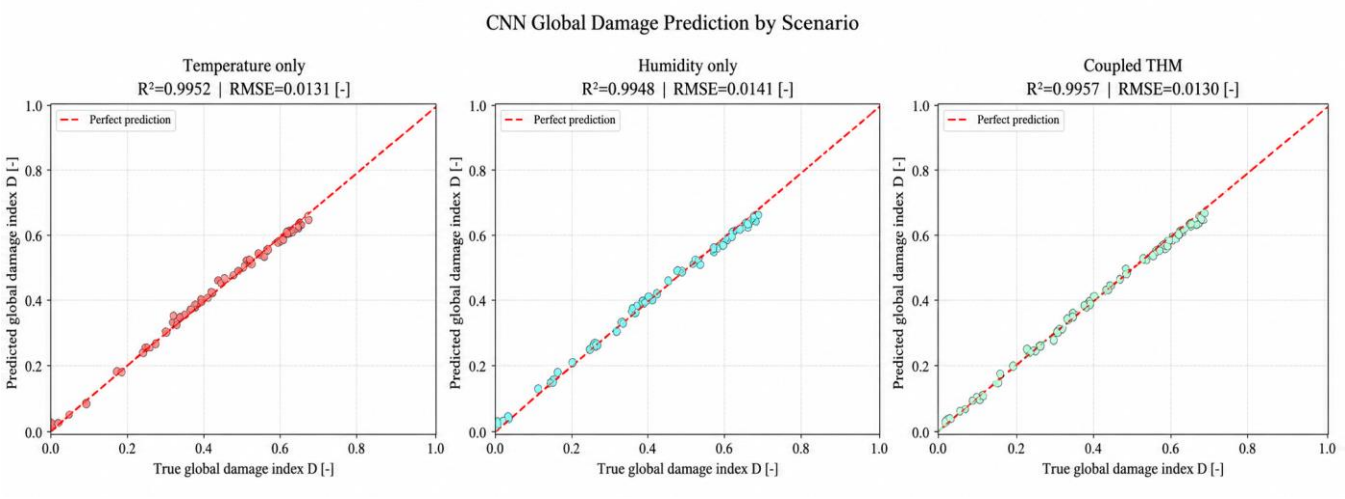

Fig. 10 Scenario-Wise regression of CNN-Predicted global damage index (D) on the independent test subset

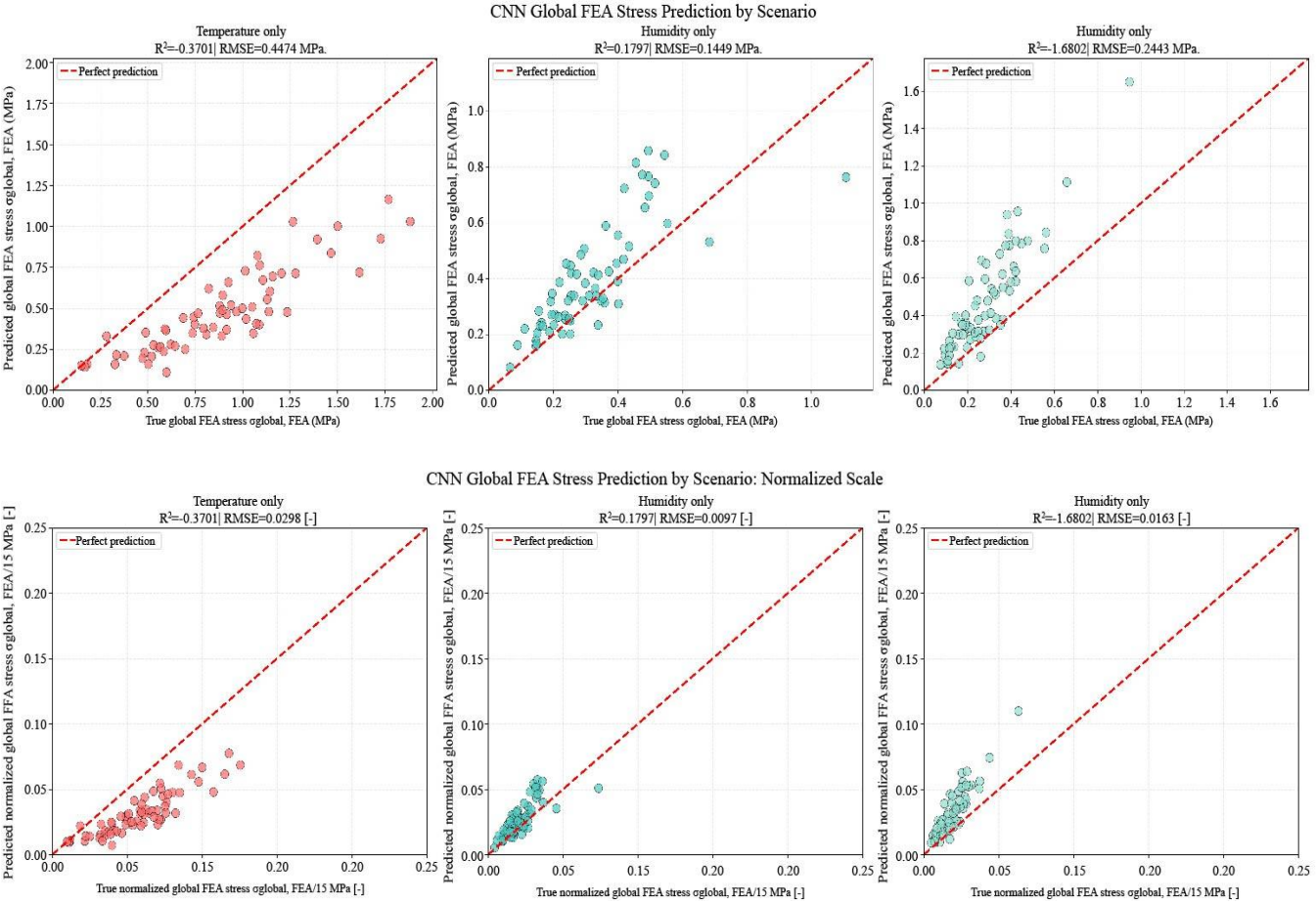

Fig. 11 Scenario-wise CNN regression of global FEA stress in physical scale (Top, MPa) and normalized scale (Bottom)

Table 4. Strain-Only analytical baseline for global damage on the independent test subset (Dimensionless)

Strain-Only Analytical Baseline	R^2	MAE	RMSE
	0.999999976	0.000026641	0.000030338

a) Strain-only analytical baseline obtained by applying Equation 4 directly to the applied-strain input of the independent test subset.

Table 5. Summary of the CNN global regression performance metrics (R^2, MAE, RMSE) evaluated overall and across the three environmental scenarios

CNN	**Global Damage (D)**	Overall	Dimensionless	R^2	0.995254338	-
				MAE	0.011098636	-
				RMSE	0.013391562	-
		Temperature Only		R^2	0.99521023	-
				MAE	0.011002456	-
				RMSE	0.013064504	-
		Humidity Only		R^2	0.994812489	-
				MAE	0.011810139	-
				RMSE	0.014075501	-
		Coupled THM		R^2	0.995690644	-
				MAE	0.010501415	-
				RMSE	0.013019171	-
	Global FEA Stress ($\sigma_{global,FEA}$)	Overall	Normalized[a)]	R^2	0.324189067	-
				MAE	0.015645562	-
				RMSE	0.020361763	-
			Physical[b)]	MAE	0.234683424	MPa
				RMSE	0.30542646	MPa
		Temperature Only	Normalized	R^2	-0.370053768	-
				MAE	0.026782164	-
				RMSE	0.029827767	-
			Physical	MAE	0.401732445	MPa
				RMSE	0.447416505	MPa
		Humidity Only	Normalized	R^2	0.179745078	-
				MAE	0.007251498	-
				RMSE	0.009658469	-
			Physical	MAE	0.108772464	MPa
				RMSE	0.144877033	MPa
		Coupled THM	Normalized	R^2	-1.680227041	-
				MAE	0.012983687	-
				RMSE	0.016289427	-
			Physical	MAE	0.194755301	MPa
				RMSE	0.244341409	MPa

a) Stress values divided by 15 MPa reference value and therefore dimensionless | b) Stress values expressed in MPa

4.6. U-Net Predictive Performance: Spatial Field Prediction

To evaluate the capacity of the U-Net architecture to predict localized structural responses from the synthetic input tensor, the model was trained using the 5-channel THM-mechanical input tensor to predict the spatial damage map and normalized FEA-derived stress field. The network was trained with a maximum of 100 epochs with an early stopping mechanism, monitoring convergence via a combined SSIM-MAE loss as the primary loss function. The final predictive accuracy of the spatial mapping was subsequently quantified across the isolated and coupled environmental scenarios using SSIM, MAE, and RMSE. The training history, scenario-specific visual comparisons between ground-truth and predicted fields for both spatial damage mapping and FEA stress fields, and the summary of the corresponding test metrics are presented, respectively, in Figures 12-14, and Table 6.

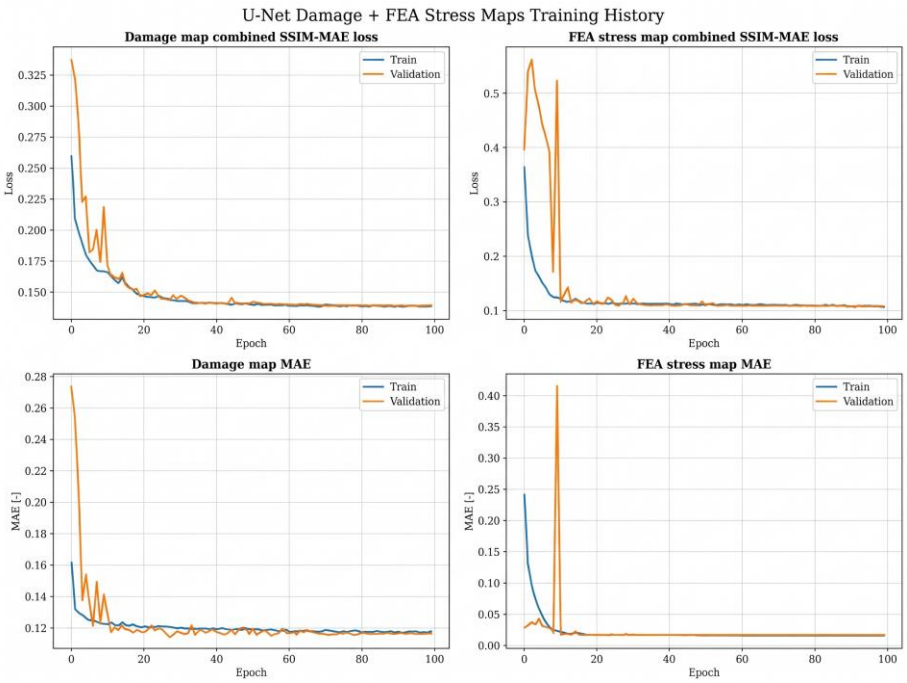

Fig. 12 U-Net training history showing the combined SSIM–MAE loss and MAE for spatial damage and FEA stress-map prediction

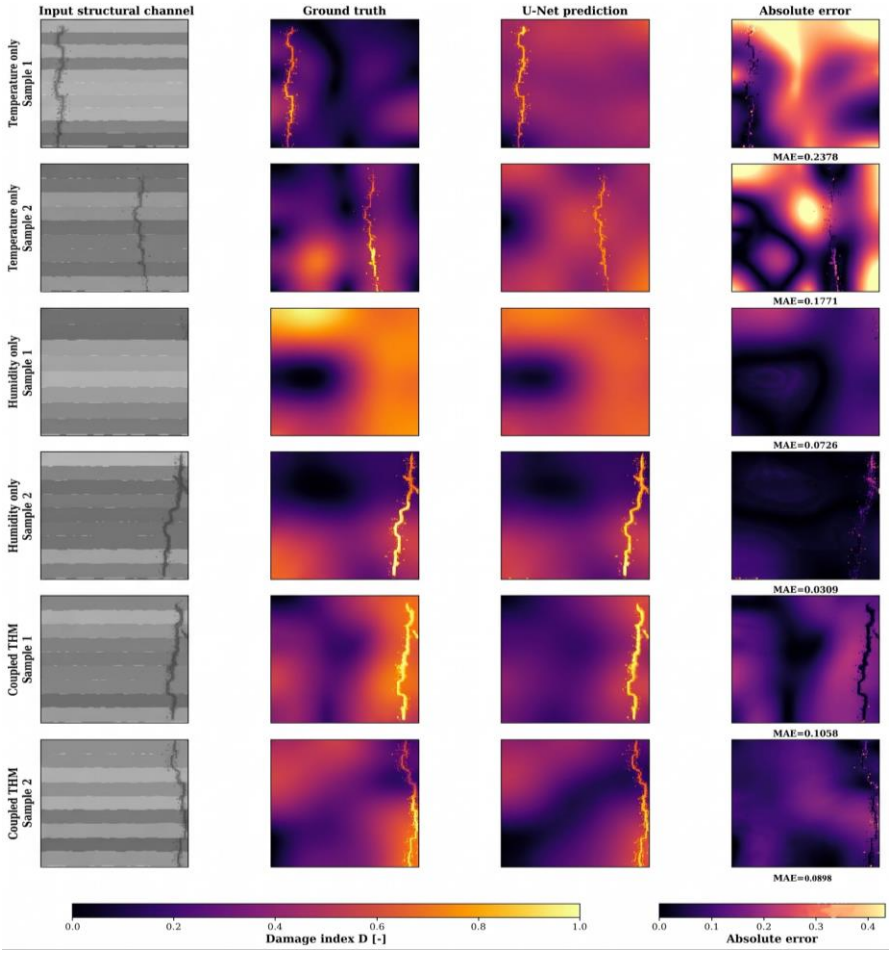

Fig. 13 Representative U-Net spatial damage predictions across the three environmental scenarios, showing the degraded structural texture channel, ground-truth damage map, predicted damage map, and absolute error

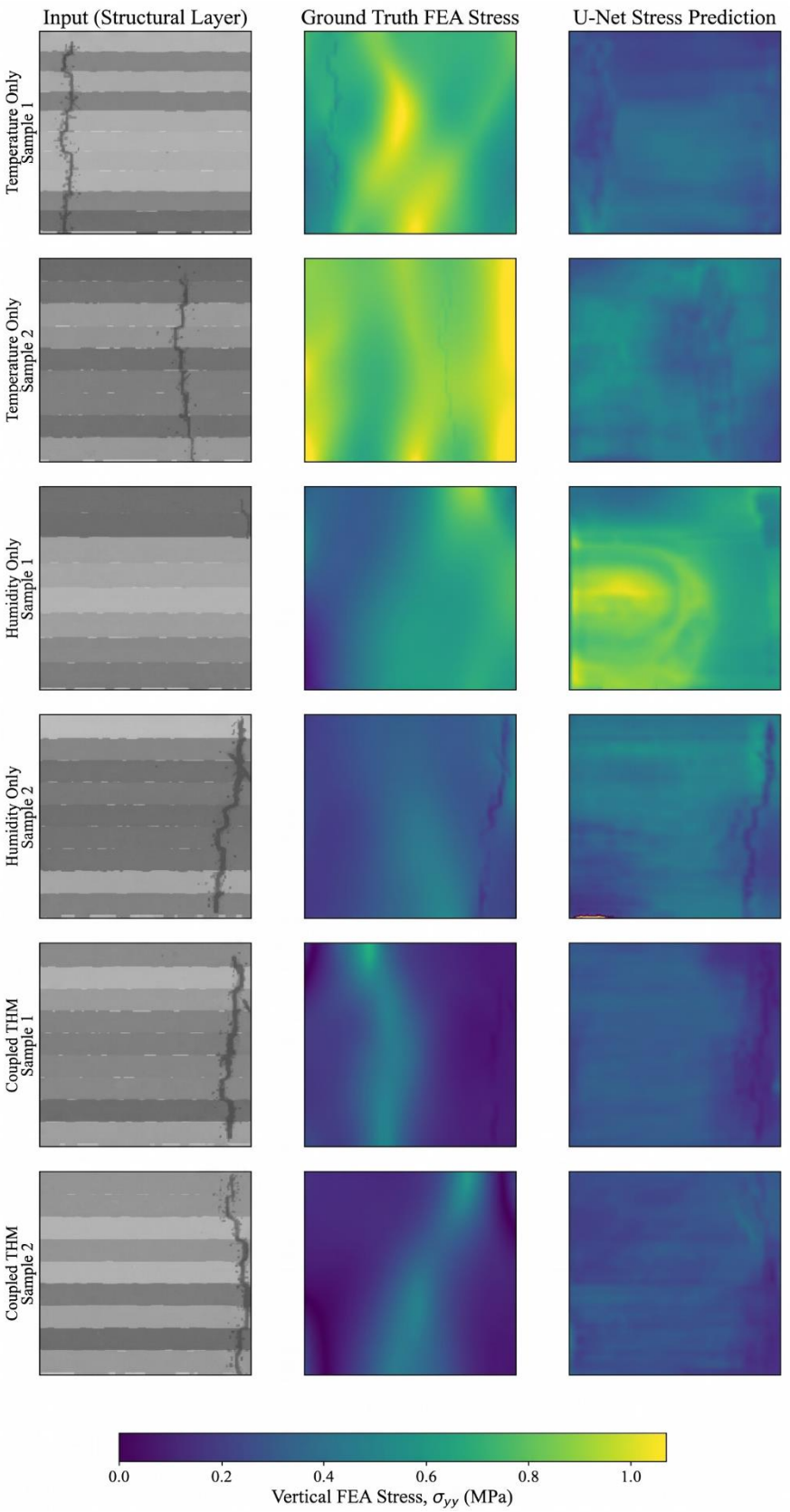

Fig. 14 Representative comparison between ground-truth FEA stress fields and U-Net-Predicted vertical FEA stress fields in MPa for the temperature-only, humidity-only, and coupled THM scenarios

Table 6. U-Net spatial prediction performance on the independent test subset, evaluated overall and across the three environmental scenarios for damage and FEA stress outputs

U-Net	**Spatial Damage Map (D)**	Overall	Dimensionless	SSIM	0.855053663	-
				MAE	0.117435947	-
				RMSE	0.165016949	-
		Temperature Only		SSIM	0.646164536	-
				MAE	0.225173473	-
				RMSE	0.262721151	-
		Humidity Only		SSIM	0.97138989	-
				MAE	0.041146509	-
				RMSE	0.05422106	-
		Coupled THM		SSIM	0.94488436	-
				MAE	0.086912595	-
				RMSE	0.101213552	-
	Spatial FEA Stress Map ($\lvert\sigma_{yy}\rvert$)	Overall	Normalized	SSIM	0.85975343	-
				MAE	0.016546883	-
				RMSE	0.026026547	-
			Physical	MAE	0.248203099	MPa
				RMSE	0.390398145	MPa
		Temperature Only	Normalized	SSIM	0.736152411	-
				MAE	0.033562262	-
				RMSE	0.039821934	-
			Physical	MAE	0.5034343	MPa
				RMSE	0.597328961	MPa
		Humidity Only	Normalized	SSIM	0.940385759	-
				MAE	0.006993709	-
				RMSE	0.014459693	-
			Physical	MAE	0.104905702	MPa
				RMSE	0.216895416	MPa
		Coupled THM	Normalized	SSIM	0.901458323	-
				MAE	0.009304145	-
				RMSE	0.015818307	-
			Physical	MAE	0.139562249	MPa
				RMSE	0.237274602	MPa

5. Discussion

5.1. Influence of Environmental Coupling on URE Mechanics

The proposed framework indicates that environmental boundary conditions can exert a nonlinear, coupled influence on the mechanical degradation of URE with the adopted synthetic model. Drawing on unsaturated soil mechanics theory, the moisture field is the dominant factor driving local weakening mechanisms: high relative humidity reduces matrix suction, which in turn diminishes apparent cohesion and inter-particle friction, accelerating spatial damage within water-rich zones. The temperature gradient acts as a secondary catalyst; temperature variations alone do not trigger catastrophic performance loss. However, under the coupled THM scenario, the simultaneous moisture and temperature-gradient contributions produce spatially heterogeneous weakened regions. The procedural crack-generation stage produces corresponding damage morphologies, including vertical and diagonal crack patterns, while the subsequent FEA stage resolves equilibrium-consistent stress redistribution and localized stress concentrations. These generated crack features are phenomenological. The combined influence of environmental attenuation, material heterogeneity, damage, and mechanical equilibrium, therefore provides the physically informed basis of the synthetic framework.

5.2. Interpretation of CNN Global Prediction Performance

The CNN demonstrated markedly different predictive performance depending on the target variable. For the global damage index (D), the model achieved very high accuracy, with an overall R^2 of 0.995, an MAE of 0.011, and an RMSE

of 0.013. However, the strain-only analytical baseline achieved an essentially exact reconstruction of this target, with $R^2 = 0.999999976$, $MAE = 2.66 \times 10^{-5}$, and $RMSE = 3.03 \times 10^{-5}$. The fact that the scalar global damage index is a deterministic function of the applied strain (as shown in Eq. 4) explains why this type of behavior was expected. Therefore, the high CNN damage prediction accuracy is an indication that the CNN was able to learn the deterministic relationship between applied strain and damage, which is contained in the 5-channel tensor that includes the applied-strain channel. Therefore, environmental and material heterogeneity cannot be seen as being independent factors influencing the scalar global damage index; instead, they can be better described through their impact on spatial damage distributions and on the equilibrium-based finite element analysis stress responses.

The evaluation of the ability of the CNN to predict the overall FEA stress ($\sigma_{global,FEA}$) was more challenging. At the overall level, the CNN achieved an R^2 of 0.324, with an MAE of 0.235 MPa and an RMSE of 0.305 MPa, however, the scenario-specific R^2 values remained lower than those obtained at the overall level and were negative for the temperature-only and coupled THM subsets. The reduced capability of the CNN to capture the complexity of the equilibrium-based stress response is due to the complicated interactions that occur between spatial variation in stiffness, environmentally induced degradation, the evolution of damage, and the redistribution of loads within the specimen.

At the global level, the CNN is able to represent some of these interactions; however, it is much more difficult to compress the spatially variable response of the FEA into a single scalar value than it is to represent the global damage index. Therefore, the results indicate that the CNN has limited ability to regress global stresses, and the negative scenario-specific R^2 values indicate that the CNN cannot be relied upon to outperform a scenario-mean baseline for the temperature-only and coupled THM subsets.

5.3. Interpretation of U-Net Spatial Prediction Performance

The U-Net architecture demonstrated excellent overall ability to predict both the spatial damage and FEA stress field. Overall performance for predicting spatial damage mapping was as follows: an overall SSIM of 0.855, with an MAE of 0.117 and an RMSE of 0.165.

While the best results were obtained for the humidity only and coupled THM scenarios (with SSIM values of 0.971 and 0.945, respectively), the temperature only scenario produced the lowest SSIM value of 0.646.

These variations indicate that the model better represented moisture-driven degradation patterns than spatial patterns related to temperature gradients alone.

The U-Net also reproduced the FEA-derived stress fields with an overall SSIM of 0.860, a normalized MAE of 0.017, and a normalized RMSE of 0.026. In physical units, the corresponding overall MAE and RMSE were 0.248 MPa and 0.390 MPa, respectively. The humidity-only and coupled THM cases again showed stronger spatial agreement, with SSIM values of 0.940 and 0.901, whereas the temperature-only case reached 0.736. These results indicate that the U-Net was able to learn the spatial organization of the equilibrium-consistent FEA stress response from the 5-channel input tensor. The network, therefore acts as a surrogate for the FEA-generated spatial response after training, rather than replacing the equilibrium formulation used to generate the reference targets.

The sensitivity analysis indicates that the structural texture channel contributes useful spatial localization information, as neutralizing this channel produced a moderate deterioration in damage-map performance. However, the prediction did not collapse when the texture information was removed, indicating that the U-Net does not depend exclusively on visible crack morphology. Because the structural texture represents the synthetically generated degraded state and contains crack features that are also reflected in the damage target, the spatial damage task is more appropriately interpreted as reconstruction of the current degradation state than as prospective prediction of future crack initiation from an initially undamaged specimen.

5.4. Literature-based Benchmarking and Limitations

Because the present study is based on a synthetic THM-informed data generation framework, no new laboratory experiments were conducted. Therefore, the validation strategy adopted here should not be interpreted as direct experimental validation. Instead, the proposed framework was evaluated through two complementary levels: internal numerical evaluation using the independent test subset of the generated dataset, and external physical-consistency benchmarking against published THM studies on URE.

The internal evaluation assessed whether the neural networks were able to reproduce the relationships generated by the synthetic physics-informed engine. The CNN model was evaluated using regression indicators, including the coefficient of determination, root mean square error, and mean absolute error, while the U-Net model was evaluated using image-based and pixel-wise metrics, including structural similarity, root mean square error, and mean absolute error.

This phase of the study evaluates the potential of the proposed architecture to predict future performance. It will not, however, be sufficient evidence to prove that the architecture is experimentally valid. Therefore, an additional evaluation is needed to compare the current data set with other published thermal mechanical trends.

The external benchmark studies chosen were those of Zhang and Nowamooz [13, 14], as these two studies are the closest to the numerical THM investigations on URE walls. The current study does not match the wall geometry, boundary conditions, time-dependent drying process, nor the finite-element equilibrium formulation employed in either study. Therefore, a direct numerical comparison of the absolute stress levels wouldn't be meaningful. Rather, the results of our study were compared to the previous studies based on physical directionality and consistency. In this context, th proposed framework is considered consistent with the THM literature if it demonstrates the same tendencies as the previous studies: increased moisture/humidity-related degradation results in increased damage predictions and lower FEA global stress responses; reduced moisture/humidity-related degradation results in better mechanical responses; temperature gradients result in spatially varying response distributions due to their effect on hygrothermal redistribution; and spatial variations in compaction/stiffness result in local stress redistribution and non-uniform damage. This comparison is summarized in Table 7. The agreement is therefore qualitative and mechanistic rather than experimental or point-by-point numerical. The purpose is to verify that the proposed CNN and U-Net framework does not produce physically contradictory behavior when compared with published THM studies on URE walls.

The numerical framework nevertheless remains simplified. Mechanical equilibrium is enforced through a two-dimensional plane-stress FEA model, while THM effects are represented through environment-dependent stiffness degradation rather than through fully coupled heat–moisture–mechanical transport. Because generated crack morphology is present in the structural texture channel and is also reflected in the spatial damage target, some direct localization information is available to the U-Net, which should be considered when interpreting the reported spatial-damage performance. Future work should therefore include laboratory testing and higher-fidelity coupled numerical models for further calibration and validation.

5.5. Practical Implications for Structural Engineering

The findings of this study demonstrate the potential of the proposed framework as a computational support tool for the assessment of URE structures. Conventional structural evaluation may require detailed numerical simulations, laboratory testing, and material calibration, which can be time-consuming and resource-intensive. The use of the DL model will provide a surrogate method of predicting global and local degradation parameters based upon learning from FEA-generated outputs after training is complete. Therefore, this current framework is intended to be a proof-of-concept for a field-ready assessment system. The primary use of the framework will lie in demonstrating how environmental, structural, and mechanical data may be integrated into a DL surrogate to allow for prediction of damage and stress patterns. This approach has potential for applications in heritage conservation, material prototyping, and SHM once the model has been experimentally calibrated and validated.

- In-Situ Heritage Conservation: For historic earthen structures, the proposed framework could support non-destructive assessment by combining environmental and structural information with material parameters to estimate damage and stress patterns. Experimental calibration and field validation would be required before such predictions could be used for practical conservation decisions.
- Material Prototyping: The framework could support preliminary comparison of different URE material configurations under varying humidity and temperature conditions by providing surrogate predictions of their mechanical response after the model has been trained.
- SHM: With future integration of field measurements and experimental validation, the proposed approach could contribute to monitoring changes in damage and stress patterns in earthen structures under changing environmental conditions.

Table 7. Implementation-based literature benchmark used to assess the physical consistency of the proposed THM-informed DL framework

THM mechanism	Finding reported in Zhang and Nowamooz [13, 14]	Representation in the present framework	Model output affected	Validation interpretation
Relative humidity and moisture sensitivity	URE behavior is strongly influenced by relative humidity, suction, and environmental moisture conditions. Drier climatic conditions lead to slightly higher mechanical strength than wetter conditions	Relative humidity is explicitly included as one of the input channels and contributes to the local THM degradation penalty	Global FEA stress, localized damage map, normalized FEA stress field	The model directly embeds humidity-driven degradation in the synthetic THM engine. This is consistent with the literature-reported link between humidity, suction, and URE mechanical performance

Suction-related mechanical response	Increasing suction increases the unconfined compressive strength of URE, while wetting reduces stiffness and strength	The synthetic degradation formulation treats moisture-related loss of suction as a reduction in mechanical performance	Global FEA stress and localized damage/stiffness response	The model's humidity penalty is physically justified because published THM formulations link suction evolution to strength and stiffness changes in URE
Temperature field and thermal gradients	Average wall temperature is governed mainly by environmental temperature variation, while humidity and fine content have a stronger influence on hydraulic and mechanical behavior	Temperature is included as a spatial input field and contributes to the THM penalty and redistribution of local response	Localized damage map and normalized FEA stress field	Temperature is not treated as the only degradation driver; rather, it acts as a coupled environmental field that influences the spatial distribution of degradation, consistent with THM wall behavior
Material type, fine content, and compaction state	Material type, fine content, dry density, and compaction-related properties strongly influence hydraulic, thermal, and mechanical behavior	Structural texture represents spatial heterogeneity, while the initial elastic modulus is included as an additional mechanical input channel	Local stress redistribution, damage localization, and global FEA stress	The texture channel provides a simplified image-based representation of the material heterogeneity that Zhang and Nowamooz identified as important for URE THM response
Coupled THM behavior	Hydraulic, thermal, and mechanical properties of URE walls are interconnected	The synthetic engine combines humidity, temperature, structural texture, damage evolution, and stress redistribution in one coupled computational workflow	CNN global FEA stress and U-Net spatial outputs; the scalar global damage index D remains strain-defined	The framework combines THM-informed synthetic data generation with equilibrium-based 2D plane-stress FEA to generate mechanically consistent stress targets for deep-learning prediction
Mechanical capacity under environmental degradation	Pushover strength and horizontal stress capacity vary with material, geometry, vertical load, humidity, suction, and rising dampness	Global FEA stress is generated as a scalar output, while stress redistribution is generated as a spatial field	CNN-predicted global FEA stress and U-Net-predicted FEA stress map	The model translates wall-scale THM strength concepts into scalar and spatial prediction targets suitable for DL

6. Conclusion

This study proposes a new DL framework for evaluating the THM-induced degradation in URE, and establishes an integrated methodology that encompasses synthetic data generation, equilibrium-based stress analysis, deep-learning prediction, literature-based benchmarking, limitation assessment, and future research directions. An internal generation engine embedded in the framework has dynamically generated 2,000 synthetic samples, each represented by a 5-channel THM-mechanical input tensor containing temperature, relative humidity, structural texture, initial elastic modulus, and applied strain. The generated material fields were subsequently transferred to a two-dimensional plane-stress FEA model to obtain equilibrium-consistent global and spatial stress targets for CNN and U-Net training.

This study carries out comparative tests to evaluate the prediction of global damage and FEA-derived stress responses under the temperature-only, humidity-only, and coupled THM scenarios. The CNN accurately reproduced the prescribed strain-defined global damage index (D), with an R^2 value of 0.995, with an MAE of 0.011 and an RMSE of 0.013. Prediction of the global FEA stress ($\sigma_{global,FEA}$) was more challenging, with an overall R^2 of 0.324, an MAE of 0.235 MPa, and an RMSE of 0.305 MPa, indicating that the heterogeneous equilibrium-based stress response is more difficult to represent through scalar regression. The U-Net showed stronger capability for spatial prediction, achieving an overall SSIM of 0.855 for damage mapping and 0.860 for FEA stress mapping. Under the coupled THM scenario, the corresponding SSIM values reached 0.945 and 0.901, respectively. These results indicate that the U-Net can

reproduce the spatial organization of damage and FEA-derived stress fields from the 5-channel inputs, while the literature-based benchmark confirms that the predicted degradation trends remain physically consistent with previously reported THM behavior of URE.

This study has three core limitations. First, limitations related to data sources: the research framework relies solely on dynamically generated synthetic data and does not adopt measured data obtained from laboratory tests or full-scale field measurements. Second, the mechanical formulation remains simplified, as equilibrium is enforced through a two-dimensional plane-stress FEA model, while THM effects are represented through environment-dependent stiffness degradation rather than through fully coupled heat–moisture–mechanical transport. The phenomenological damage and environmental degradation formulations are therefore not calibrated to the specific micromechanical characteristics of individual URE mixtures. Third, limitations related to validation methods: the literature benchmarking method used in this study is an indirect validation approach, and direct experimental validation of predicted damage and stress profiles has not yet been completed.

Therefore, combined with the research limitations summarized in the preceding sections, this study sets direct experimental verification as the core priority for future work, which will be advanced along two major dimensions: First, prepare controlled URE specimens, set up different temperature and humidity test conditions, and compare predicted and measured deformation, damage evolution, and global mechanical response using digital image correlation and thermal imaging methods; Second, the analysis framework should be iteratively refined to incorporate time-dependent drying and moisture transport, higher-fidelity coupled THM formulations, and experimental calibration for different soil compositions, compaction states, and in-situ wall conditions.

The contribution of this work lies in combining THM-informed synthetic data generation, equilibrium-consistent FEA stress targets, and global and spatial DL prediction within a single computational framework for URE. Rather than replacing the underlying mechanics, the trained neural networks act as surrogates that approximate the FEA-derived global and spatial responses from the 5-channel inputs. The results demonstrate the potential of spatial deep-learning architectures for representing heterogeneous damage and stress patterns in earthen materials and provide a basis for subsequent experimental calibration and field-oriented development. Future work may further reduce the gap between synthetic modeling and real structures through experimental validation, constitutive model refinement, and transfer-learning strategies.

References

[1] Ahmed Abdelaal et al., "Bio-Stabilized Modular Rammed Earth Blocks for Sustainable and Aesthetic Construction," *Construction Innovation: Information Process Management*, vol. 26, no. 9, pp. 1-20, 2026. [CrossRef] [Google Scholar] [Publisher Link]

[2] Fernando Ávila, Esther Puertas, and Rafael Gallego, "Characterization of the Mechanical and Physical Properties of Unstabilized Rammed Earth: A Review," *Construction and Building Materials*, vol. 270, 2021. [CrossRef] [Google Scholar] [Publisher Link]

[3] Taiwo Sesay et al., "Bio-Based Stabilization of Natural Soil for Rammed Earth Construction: A Review on Mechanical and Water Durability Performance," *Polymers*, vol. 17, no. 9, pp. 1-37, 2025. [CrossRef] [Google Scholar] [Publisher Link]

[4] Maqi Jiang et al., "Thermal and Humidity Performance Test of Rammed-Earth Dwellings in Northwest Sichuan during Summer and Winter," *Materials*, vol. 16, no. 18, pp. 1-20, 2023. [CrossRef] [Google Scholar] [Publisher Link]

[5] Fernando Ávila et al., "Experimental and Numerical Evaluation of the Compressive and Shear Behavior of Unstabilized Rammed Earth," *Materials and Structures*, vol. 56, no. 7, pp.1-14, 2023. [CrossRef] [Google Scholar] [Publisher Link]

[6] Fernando Ávila et al., "Multiscale Experimental Framework for the Characterization of Unstabilized Rammed Earth," *Applied Sciences*, vol. 16, no. 12, pp. 1-23, 2026. [CrossRef] [Google Scholar] [Publisher Link]

[7] Christoph Waibel et al., "Estimating Hygrothermal Properties of a Rammed Earth Construction from Short-horizon Measurements with ML," *IOP Conference Series: Earth and Environmental Science: Sustainable Built Environment Conference*, Zurich, Switzerland, vol. 1554, pp. 1-11, 2025. [CrossRef] [Google Scholar] [Publisher Link]

[8] P. A. Jaquin et al., "The Strength of Unstabilised Rammed Earth Materials," *Geotechnique*, vol. 59, no. 5, pp. 487-490, 2009. [CrossRef] [Google Scholar] [Publisher Link]

[9] Christopher Beckett, and Charles Augarde, "The Effect of Relative Humidity and Temperature on the Unconfined Compressive Strength of Rammed Earth," *Unsaturated Soils: Research and Applications*, vol. 1, pp. 287-292, 2012. [CrossRef] [Google Scholar] [Publisher Link]

[10] Quoc-Bao Bui et al., "Effect of Moisture Content on the Mechanical Characteristics of Rammed Earth," *Construction and Building Materials*, vol. 54, pp. 163-169, 2014. [CrossRef] [Google Scholar] [Publisher Link]

[11] Qinglong Gao et al., "Prediction of Wall and Indoor Hygrothermal Properties of Rammed Earth Folk House in Northwest Sichuan," *Energies*, vol. 15, no. 5, pp. 1-16, 2022. [CrossRef] [Google Scholar] [Publisher Link]

[12] Piotr Kosiński, Wojciech Jabłoński, and Krystian Patyna, "Parametric Analysis of Rammed Earth Walls in the Context of the Thermal Protection of Environmentally Friendly Buildings," *Sustainability*, vol. 17, no. 15, pp. 1-19, 2025. [CrossRef] [Google Scholar] [Publisher Link]

[13] Xiang Zhang, and Hossein Nowamooz, "Thermo-Hydro-Mechanical (THM) behavior of Unstabilized Rammed Earth (URE) Wall Submitted to Environmental and Mechanical Loadings," *Materials and Structures*, vol. 54, no. 5, 2021. [CrossRef] [Google Scholar] [Publisher Link]

[14] Xiang Zhang, and Hossein Nowamooz, "Factors Influencing the Thermo-Hydro-Mechanical Behavior of Unstabilized Rammed Earth Walls," *Materials*, vol. 15, no. 24, pp. 1-25, 2022. [CrossRef] [Google Scholar] [Publisher Link]

[15] Mohsen Azimi, Armin Dadras Eslamlou, and Gokhan Pekcan, "Data-Driven Structural Health Monitoring and Damage Detection through Deep Learning: State-of-the-Art Review," *Sensors*, vol. 20, no. 10, pp. 1-34, 2020. [CrossRef] [Google Scholar] [Publisher Link]

[16] Jing Jia, and Ying Li, "Deep Learning for Structural Health Monitoring: Data, Algorithms, Applications, Challenges, and Trends," *Sensors*, vol. 23, no. 21, pp. 1-43, 2023. [CrossRef] [Google Scholar] [Publisher Link]

[17] John Mark Go Payawal, and Dong-Keon Kim, "Image-Based Structural Health Monitoring: A Systematic Review," *Applied Sciences*, vol. 13, no. 2, pp. 1-29, 2023. [CrossRef] [Google Scholar] [Publisher Link]

[18] Hafsa Matich, Jamal Attmani, and Hajar Mousannif, "Enhancing Crack Detection and Severity Assessment in Historical Tabiya Basins using U-Net and Adaptive Thresholding," *Frontiers in Artificial Intelligence*, vol. 9, pp. 1-19, 2026. [CrossRef] [Google Scholar] [Publisher Link]

[19] Piotr Narloch et al., "Predicting Compressive Strength of Cement-Stabilized Rammed Earth Based on SEM Images Using Computer Vision and Deep Learning," *Applied Sciences*, vol. 9, no. 23, pp. 1-14, 2019. [CrossRef] [Google Scholar] [Publisher Link]

[20] Olaf Ronneberger, Philipp Fischer, and Thomas Brox, "U-Net: Convolutional Networks for Biomedical Image Segmentation," *18th International Conference, Medical Image Computing and Computer-Assisted Intervention – MICCAI 2015*, Munich, Germany, pp. 234-241, 2015. [CrossRef] [Google Scholar] [Publisher Link]

[21] Hessam Kaveh, and Reda Alhajj, "Recent Advances in Crack Detection Technologies for Structures: A Survey of 2022-2023 Literature," *Frontiers in Built Environment*, vol. 10, pp. 1-22, 2024. [CrossRef] [Google Scholar] [Publisher Link]

[22] Fangzheng Lin et al., "Crack Semantic Segmentation using the U-Net with Full Attention Strategy," *arXiv preprint*, pp. 1-10, 2020. [CrossRef] [Google Scholar] [Publisher Link]

[23] Qiong Zhang et al., "Improved U-net Network Asphalt Pavement Crack Detection Method," *PLOS ONE*, vol. 19, no. 5, pp. 1-21, 2024. [CrossRef] [Google Scholar] [Publisher Link]

[24] Thibault Delage, Sanaa Zannane, and Thibaut Neveux, "Metamodeling of Chemical Engineering Unit Operations using Kriging and Prediction Error Estimation," *32nd European Symposium on Computer Aided Process Engineering*, vol. 51, pp. 535-540, 2022. [CrossRef] [Google Scholar] [Publisher Link]

[25] Maliki Moustapha et al., "Comparative Study of Kriging and Support Vector Regression for Structural Engineering Applications," *ASCE-ASME Journal of Risk and Uncertainty in Engineering Systems, Part A: Civil Engineering*, vol. 4, no. 2, 2018. [CrossRef] [Google Scholar] [Publisher Link]

[26] Iván Negrin, Moacir Kripka, and Víctor Yepes, "Metamodel-Assisted Design Optimization in the Field of Structural Engineering: A Literature Review," *Structures*, vol. 52, pp. 609-631, 2023. [CrossRef] [Google Scholar] [Publisher Link]

[27] Madhuri Gonthina et al., "Deep CNN-based Concrete Cracks Identification and Quantification using Image Processing Techniques," *Asian Journal of Civil Engineering*, vol. 24, no. 3, pp. 727-740, 2023. [CrossRef] [Google Scholar] [Publisher Link]

[28] Edisson Alberto Moscoso Alcantara, and Taiki Saito, "Convolutional Neural Network-Based Rapid Post-Earthquake Structural Damage Detection: Case Study," *Sensors*, vol. 22, no. 17, pp. 1-22, 2022. [CrossRef] [Google Scholar] [Publisher Link]

[29] Yulin Zhan et al., "Application of Convolutional Neural Network in Random Structural Damage Identification," *Structures*, vol. 29, pp. 570-576, 2021. [CrossRef] [Google Scholar] [Publisher Link]

[30] D. H. Hubel, and T. N. Wiesel, "Receptive Fields, Binocular Interaction and Functional Architecture in the Cat's Visual Cortex," *The Journal Physiology*, vol. 160, no. 1, pp. 106-154, 1962. [CrossRef] [Google Scholar] [Publisher Link]

[31] Alex Krizhevsky, Ilya Sutskever, and Geoffrey E. Hinton, "ImageNet Classification with Deep Convolutional Neural Networks," *Communications of the ACM*, vol. 60, no. 6, pp. 84-90, 2017. [CrossRef] [Google Scholar] [Publisher Link]

[32] Md. Himel Reza et al., "A Comprehensive Review of Convolutional Neural Networks: Foundations, Enhancements and Applications, Enhancements and Applications," *Neural Computing and Applications*, vol. 38, no. 4, pp. 1-46, 2026. [CrossRef] [Google Scholar] [Publisher Link]

[33] Iqbal H. Sarker, "Deep Learning: A Comprehensive Overview on Techniques, Taxonomy, Applications and Research Directions," *SN Computer Science*, vol. 2, no. 6, pp. 1-20, 2021. [CrossRef] [Google Scholar] [Publisher Link]

[34] Andrew Mann, and Surya R. Kalidindi, "Development of a Robust CNN Model for Capturing Microstructure-Property Linkages and Building Property Closures Supporting Material Design," *Frontiers in Materials*, vol. 9, pp. 1-14, 2022. [CrossRef] [Google Scholar] [Publisher Link]

[35] Vijay Badrinarayanan, Alex Kendall, and Roberto Cipolla, "SegNet: A Deep Convolutional Encoder-Decoder Architecture for Image Segmentation," *IEEE Transactions on Pattern Analysis and Machine Intelligence*, vol. 39, no. 12, pp. 2481-2495, 2015. [CrossRef] [Google Scholar] [Publisher Link]

[36] João Carreira, and Andrew Zisserman, "Quo Vadis, Action Recognition? A New Model and the Kinetics Dataset," *2017 IEEE Conference on Computer Vision and Pattern Recognition (CVPR)*, Honolulu, HI, USA, pp. 4724-4733, 2017. [CrossRef] [Google Scholar] [Publisher Link]

[37] Sean Bell, and Kavita Bala, "Learning Visual Similarity for Product Design with Convolutional Neural Networks," *ACM Transactions on Graphics*, vol. 34, no. 4, pp. 1-10, 2015. [CrossRef] [Google Scholar] [Publisher Link]

[38] H. Fathipoor, R. Shah-Hosseini, and H. Arefi, "Crop and Weed Segmentation On Ground-Based Images Using Deep Convolutional Neural Network," *ISPRS Annals of the Photogrammetry, Remote Sensing and Spatial Information Sciences*, vol. X-4-W1-2022, pp. 195-200, 2023. [CrossRef] [Google Scholar] [Publisher Link]

[39] Ian Goodfellow, Yoshua Bengio, and Aaron Courville, *Deep Learning*, Adaptive Computation and Machine Learning Series, MIT Press, pp. 1-800, 2016. [Google Scholar] [Publisher Link]

[40] Qingchen Zhang et al., "A Survey on Deep Learning for Big Data," *Information Fusion*, vol. 42, pp. 146-157, 2018. [CrossRef] [Google Scholar] [Publisher Link]

[41] Momojit Biswas et al., "Microstructural Segmentation using a Union of Attention guided U-Net Models with Different Color Transformed Images," *Scientific Reports*, vol. 13, pp. 1-14, 2023. [CrossRef] [Google Scholar] [Publisher Link]

[42] Wubiao Zhu et al., "CrackNet: A Novel Multi-Scale Architecture for Crack Segmentation," *PLOS One*, vol. 21, no. 4, pp. 1-24, 2026. [CrossRef] [Google Scholar] [Publisher Link]

[43] Haoran Lu et al., "Half-UNet: A Simplified U-Net Architecture for Medical Image Segmentation," *Frontiers in Neuroinformatics*, vol. 16, pp. 1-10, 2022. [CrossRef] [Google Scholar] [Publisher Link]

[44] Hao Dong et al., "Automatic Brain Tumor Detection and Segmentation Using U-Net Based Fully Convolutional Networks," *21st Annual Conference Medical Image Understanding and Analysis*, Edinburgh, UK, pp. 506-517, 2017. [CrossRef] [Google Scholar] [Publisher Link]

[45] Olivier Bernard et al., "Deep Learning Techniques for Automatic MRI Cardiac Multi-Structures Segmentation and Diagnosis: Is the Problem Solved?," *IEEE Transactions on Medical Imaging*, vol. 37, no. 11, pp. 2514-2525, 2018. [CrossRef] [Google Scholar] [Publisher Link]

[46] Thorsten Falk et al., "U-Net: Deep Learning for Cell Counting, Detection, and Morphometry," *Nature Methods*, vol. 16, no. 1, pp. 67-70, 2019. [CrossRef] [Google Scholar] [Publisher Link]

[47] Abdul Basit, Muhammad A. Siddique, and M. Saquib Sarfraz, "Deep Learning Based Oil Spill Classification Using Unet Convolutional Neural Network," *2021 IEEE International Geoscience and Remote Sensing Symposium IGARSS*, Brussels, Belgium, pp. 3491-3494, 2021. [CrossRef] [Google Scholar] [Publisher Link]

[48] JongCheol Pyo et al., "Generalization of U-Net Semantic Segmentation for Forest Change Detection in South Korea Using Airborne Imagery," *Forests*, vol. 13, no. 12, pp. 1-18, 2022. [CrossRef] [Google Scholar] [Publisher Link]

[49] Yanan Guo et al., "Cloud Detection for Satellite Imagery Using Attention-Based U-Net Convolutional Neural Network," *Symmetry*, vol. 12, no. 6, pp. 1-15, 2020. [CrossRef] [Google Scholar] [Publisher Link]

[50] Domen Tabernik et al., "Segmentation-based Deep-Learning Approach for Surface-Defect Detection," *Journal of Intelligent Manufacturing*, vol. 31, no. 3, pp. 759-776, 2020. [CrossRef] [Google Scholar] [Publisher Link]

[51] Vivian Wen Hui Wong et al., "Segmentation of Additive Manufacturing Defects Using U-Net," *Journal of Computing and Information Science in Engineering*, vol. 22, no. 3, pp. 1-9, 2022. [CrossRef] [Google Scholar] [Publisher Link]

[52] Imon Mahbub et al., "infraCrackNet: Automated Crack Detection in Infrastructure Using U-Net with Dataset Preparation, Manual Labeling, and Segmentation Performance," *2025 14th International Conference on Educational and Information Technology (ICEIT)*, Guangzhou, China, pp. 21-26, 2025. [CrossRef] [Google Scholar] [Publisher Link]

[53] Patrick Nicholas Hadinata et al., "Crack Detection on Concrete Surfaces Using Deep Encoder-Decoder Convolutional Neural Network: A Comparison Study Between U-Net and DeepLabV3+," *Journal of the Civil Engineering Forum*, vol. 7, no. 3, pp. 323-334, 2021. [CrossRef] [Google Scholar] [Publisher Link]

[54] Ali Sarhadi et al., "Optimizing Concrete Crack Detection: An Attention-Based SWIN U-Net Approach," *IEEE Access*, vol. 12, pp. 77575-77585, 2024. [CrossRef] [Google Scholar] [Publisher Link]

[55] Md. Al-Masrur Khan, Seong-Hoon Kee, and Abdullah-Al Nahid, "Vision-Based Concrete-Crack Detection on Railway Sleepers Using Dense U-Net Model," *Algorithms*, vol. 16, no. 12, pp. 1-18, 2023. [CrossRef] [Google Scholar] [Publisher Link]

[56] Ju Huyan et al., "CrackU-Net: A Novel Deep Convolutional Neural Network for Pixelwise Pavement Crack Detection," *Structural Control and Health Monitoring*, vol. 27, pp. 1-19, 2020. [CrossRef] [Google Scholar] [Publisher Link]

[57] Y. LeCun et al., "Backpropagation Applied to Handwritten Zip Code Recognition," *Neural Computation*, vol. 1, no. 4, pp. 541-551, 1989. [CrossRef] [Google Scholar] [Publisher Link]

[58] Bin Jiang et al., "Hygrothermal Performance of Rammed Earth Wall in Tibetan Autonomous Prefecture in Sichuan Province of China," *Building and Environment*, vol. 181, 2020. [CrossRef] [Google Scholar] [Publisher Link]

[59] J. Mazars, and G. Pijaudier-Cabot, "Continuum Damage Theory—Application to Concrete," *Journal of Engineering Mechanics*, vol. 115, no. 2, pp. 345-365, 1989. [CrossRef] [Google Scholar] [Publisher Link]

[60] Gordon A. Fenton, and D. V. Griffiths, *Risk Assessment in Geotechnical Engineering*, General & Introductory Civil Engineering & Construction, Wiley, pp. 1-480, 2008. [CrossRef] [Google Scholar] [Publisher Link]

[61] Erik Vanmarcke, *Random Fields: Analysis and Synthesis*, World Scientific, pp. 1-364, 2010. [CrossRef] [Google Scholar] [Publisher Link]

[62] Jean Lemaitre, "A Continuous Damage Mechanics Model for Ductile Fracture," *Journal of Engineering Materials and Technology*, vol. 107, no. 1, pp. 83-89, 1985. [CrossRef] [Google Scholar] [Publisher Link]

[63] Quoc-Bao Bui, and Jean-Claude Morel, "First Exploratory Study on the Ageing of Rammed Earth Material," *Materials*, vol. 8, no. 1, pp. 1-15, 2015. [CrossRef] [Google Scholar] [Publisher Link]

[64] Luisa María Gil-Martín, Manuel Alejandro Fernández-Ruiz, and Enrique Hernández-Montes, "Mechanical Characterization and Elastic Stiffness Degradation of Unstabilized Rammed Earth," *Journal of Building Engineering*, vol. 56, pp. 1-11, 2022. [CrossRef] [Google Scholar] [Publisher Link]

[65] A. Koutous, and E. Hilali, "Compression Stress-Strain Curve of Rammed Earth: Measuring and Modelling," *Results in Engineering*, vol. 18, pp. 1-16, 2023. [CrossRef] [Google Scholar] [Publisher Link]

[66] Lorenzo Miccoli, Urs Müller, and Patrick Fontana, "Mechanical Behaviour of Earthen Materials: A Comparison between Earth Block Masonry, Rammed Earth and Cob," *Construction and Building Materials*, vol. 61, pp. 327-339, 2014. [CrossRef] [Google Scholar] [Publisher Link]